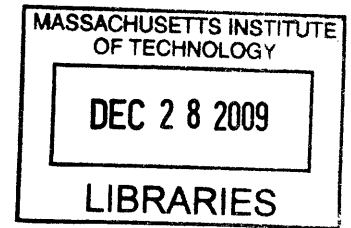


Nonlinear Effects on Interfacial Wave Growth into Slug Flow

by

Bryce K. Campbell

B.S., Drexel University (2007)



Submitted to the Department of Mechanical Engineering
in partial fulfillment of the requirements for the degree of

Masters of Science in Mechanical Engineering

at the

ARCHIVES

MASSACHUSETTS INSTITUTE OF TECHNOLOGY

September 2009

© Massachusetts Institute of Technology 2009. All rights reserved.

Author

Department of Mechanical Engineering
August 21, 2009

Certified by

Yuming Liu
Principal Research Scientist
Thesis Supervisor

Accepted by

David E. Hardt
Chairman, Department Committee on Graduate Theses

Nonlinear Effects on Interfacial Wave Growth into Slug Flow

by

Bryce K. Campbell

Submitted to the Department of Mechanical Engineering
on August 21, 2009, in partial fulfillment of the
requirements for the degree of
Masters of Science in Mechanical Engineering

Abstract

It is known that when two fluids flow through a horizontal channel, depending on the relative velocity between the two fluids, two different instability mechanisms can create initial wave disturbances on the interface: the classic Kelvin-Helmholtz instability or shear induced instability. These instability mechanisms, which affect the initial growth of the disturbances on the interface, are well understood; however, the subsequent nonlinear evolution and the effects of wave resonances on the interface remain a subject of interest and will be the focus of this study.

The Kelvin-Helmholtz (KH) instability is the traditional model for predicting interfacial instability in stratified flows. This linear instability occurs when the lower phase inertia and the pressure from the upper phase overcome the stabilizing effects of gravity and surface tension. This mechanism is most unstable to short waves and does not allow for modal interactions. When nonlinearity is included, additional second-order sum- and difference-wavenumber modes as well as higher harmonics must be accounted for. Given an initial spectrum of stable modes, sum-wavenumber modes and higher harmonics are generated due to nonlinear wave-wave interactions, which can be unstable to KH. The generated second-order difference-wavenumber modes are stable to KH. For certain combinations of wave modes, we found that there exist simultaneous coupled second-harmonic (overtone) and triad resonances. Due to the second harmonic resonance, energy from the KH unstable second harmonic is transferred to the first harmonic. Meanwhile, this first harmonic, which is involved in a triad resonance, transfers its energy to the other two (stable) wave modes. These coupled resonant wave-wave interactions result in rapid growth of long wave components on the interface.

For flows which are KH stable; the shear instability can cause the growth of relatively short waves on the interface. As in the case of KH instability, the overtone and triad resonances can also occur. The overtone resonance transfers energy from the dominant unstable mode to its subharmonic (creating a period doubling phenomenon). Similarly the triad resonance enables the transfer of energy from unstable mode(s) to stable mode(s). These resonant wave-wave interactions provide a mechanism for the growth of long waves by taking energy from (relatively short) unstable

waves.

This work considers nonlinear wave-wave interactions and interfacial wave resonances in a two-fluid stratified flow through a horizontal channel for the purpose of understanding mechanisms capable of generating slug flow. Stable resonances are considered and a nonlinear solution is obtained through the method of multiple scales. In addition to this, an efficient high-order spectral method is developed for the simulation of the generation and nonlinear evolution of interfacial waves. This numerical method is based on a potential flow formulation which includes normal viscous stresses and a pressure forcing term at the interface respectively for modeling of the damping effect and surface shear effect by the upper fluid. The method is capable of accounting for the nonlinear interactions of a large number of wave components in a broadband spectrum, and obtains an exponential convergence of the solution with the number of spectral modes and interaction order.

Direct comparisons between the numerical simulations and the multiple scale analytic solutions are made. Excellent agreement is found between the two methods. The numerical simulations are also compared against existing laboratory experiments. Good agreement between them is observed. The findings in this study improve the understanding of the underlying mechanisms which can cause short waves to evolve into large amplitude liquid slugs through nonlinear wave-wave interactions.

Thesis Supervisor: Yuming Liu
Title: Principal Research Scientist

Acknowledgments

I would like to convey my deepest thanks to all those that participated in this effort. I am profoundly grateful to my advisor, Dr. Yuming Liu, for his help in leading me through this process. His guidance, encouragement, and unbelievable patience has made this an invaluable learning experience for me, for which I shall always be thankful. I am deeply indebted to Professor Dick Yue for allowing me to become a member of this research group and participate in the many opportunities that MIT has to offer. I would also like to thank Dr. Kelli Hendrickson and the other members of the VFRL. Without their support and friendship, this would not have been such an amazing experience.

Most of all, I would like to thank my family. To my mother, who taught me to be curious and passionate about learning and to my father for showing me how exciting it can be to study hard problems. Without their unwavering support and encouragement, I know without a doubt that I would not be the person that I am today. For this, I am eternally grateful.

Funding for this work was provided by Chevron Corporation and the Office of Naval Research.

Contents

1	Introduction	13
2	Theoretical Analysis	17
2.1	Fully Nonlinear Governing Equations	17
2.2	Linear Solution	19
2.3	Weakly Nonlinear Formulation	21
2.4	Regular Perturbation Solution for Nonlinear Resonant Wave-Wave Interactions	23
2.5	Multiple-Scale Analysis for Resonant Wave-Wave Interactions	26
2.5.1	Properties of Interaction Equations	29
3	Numerical Simulation	31
3.1	Mathematical Formulation of a High Order Spectral Method	31
3.2	Validation of the Numerical Method	36
4	Kelvin-Helmholtz Flows	39
4.1	Kelvin-Helmholtz Stable Flows	39
4.1.1	Comparison of Regular Perturbation to Multi-Scale Solution .	40
4.1.2	Effect of Wave Steepness	41
4.1.3	Verification of Special Properties	43
4.1.4	Near Resonant Interactions	43
4.1.5	Effect of Surface Tension and Normal Viscous Stresses	46
4.2	Kelvin-Helmholtz Unstable Flows	47

4.2.1	Triad Resonance	48
4.2.2	Second Harmonic Resonance For Unstable Flows	50
4.2.3	Combined Triad and Second Harmonic Resonance	52
5	Comparisons to Experiments Containing Unstable Resonant Wave- Wave Interactions	57
6	Discussion and Conclusions	63
A	Convergence Test Results	67

List of Figures

4-1	Comparison of the dimensionless amplitudes of the resonant mode determined by: regular(--) and multi-scale (-) perturbation method with the $\hat{a}_1(0) = \hat{a}_2(0) = 10^{-5}$ and $a_3(0) = 0$	41
4-2	Validation of nondimensional modal amplitudes calculated by (-)multi-scale solution and (-) numerical method for $\hat{a}_1(0) = \hat{a}_2(0) = \hat{\eta}_0$ where in: (a) $\hat{\eta}_0 = 5 \times 10^{-6}\text{m}$, (b) $\hat{\eta}_0 = 1 \times 10^{-5}\text{m}$, (c) $\hat{\eta}_0 = 5 \times 10^{-5}\text{m}$, (d) $\hat{\eta}_0 = 7.5 \times 10^{-5}\text{m}$	42
4-3	Validation of constant relative phases between the resonant modes where (a) is the exact numerical solution, (b) the magnitude of the amplitudes, and (c) shows the phases of each of the modes	44
4-4	Effect of the detuning parameter on near resonant interactions. Case (a) comparison between (-)"exact resonance" and (-) near resonance for $U_u = 3.48 \frac{\text{m}}{\text{s}}$ with $(\varepsilon\sigma \approx 0.0331232)$, (b) Comparison between (-) HOS solution and (-) multi-scale solution for the near resonance solution with larger detuning $(\varepsilon\sigma = 0.07335)$ for $U_u = 3.45 \frac{\text{m}}{\text{s}}$	45
4-5	Effect of the normal viscous stresses on triad interactions for air water flow with $\mu_u = 10^{-3} \frac{\text{N-s}}{\text{m}^2}$, $\mu_l = 1.8 \times 10^{-5} \frac{\text{N-s}}{\text{m}^2}$ and $k_1 = 1$, $k_2 = 60$, and $k_3 = 59$	47
4-6	Unstable Triad Resonance with k_1 and k_3 stable and k_2 being unstable to the KH mechanism	49
4-7	Effect of second harmonic resonance with $2k_1$ component being linearly unstable. In these trials k_1 -mode is (a) linearly unstable (b) linearly stable to the KH mechanism	51

4-8	Time trace of the second harmonic resonance with both k_1 and $2k_1$ being linearly unstable to KH	51
4-9	Combined triad and (a) only the original triad components, (b) sum-mode $(k_1 + k_2)$, (c) k_1 -mode's second harmonic $(2k_1)$, (d) k_2 -mode's second harmonic $(2k_2)$	53
4-10	Combined resonance in which all second order components $k_1, k_2, 2k_1, k_1 + k_2, 2k_2$ are included	55
4-11	Energy transfer mechanism due to resonant interactions	56
5-1	Dimensionless HOS simulation corresponding to Figure 3 from Jurman [10] with dominant wave mode $k = 49$	59
5-2	Dimensionless HOS simulation corresponding to Figure 7 from Jurman [10] with dominant wavemode $k = 79$	61
5-3	Dimensionless HOS simulation corresponding to Figure 9 from Jurman [10] with dominant wavemode $k = 86$	62

List of Tables

A.1	Convergence of the Frequency (ω_R) with Grid Refinement	67
A.2	Convergence of the Frequency (ω_R) with Time Step Refinement . . .	67
A.3	Convergence of the Growth Rate (ω_I) with Grid Refinement	68
A.4	Convergence of the Growth Rate (ω_I) with Time Step Refinement . .	68

Chapter 1

Introduction

A multiphase flow is a flow which involves some combination of solids, liquids, and gases. Many industrial applications involve the transport of multiphase flows through pipes with applications including boilers, condensers, air conditioners, offshore oil pipelines, etc. While the mixture is in transit, it is possible for the flow to exist in a number of unique hydrodynamic states including stratified, bubbly, annular, and slug flow. These flow regimes produce significant challenges in the transportation, separation, and processing of the flow. Being able to predict which hydrodynamic state the flow is in and also the conditions under which flow regime transition(s) will occur is of vital importance to the accurate modeling of multiphase transport. For gas-heavy liquid flows, the principal flow regime is slug flow. This particular flow arises when short waves, which form at the interface of the two fluids, become unstable and grow into long, large amplitude waves which eventually bridge the pipe diameter and trap long bubbles of gas within the fluid. The existence of slugs has been well documented experimentally over the past forty years, but determining the conditions under which the flow transitions from a stratified state to slug flow remains an active subject of research.

There is a rich collection of literature dedicated to defining the criteria for the transition to slug flow. The majority of the early work on slug prediction was based on modifying the classical Kelvin-Helmholtz stability criteria for infinitesimal waves at the interface of a stratified flow. Various physical features such as experimental

correlations for the interfacial friction, normal viscous stresses, long wavelength assumptions, and ad hoc empirical corrections (which are believed to represent nonlinear contributions) have been added to try and better predict slug formation. A few examples of such works includes Wallis and Dobson [20], Lin and Hanratty [12], Barnea and Taitel [2], and Funada and Joseph [7]. Attempts were made to try and improve stability predictions by examining the effects of finite-amplitude waves. Such works were conducted by Kordyban and Ranov [11], Taitel and Dukler [19], and Mishima and Ishii [16]. While these approaches did attempt to account for nonlinear effects, the analysis was incomplete because the formulation required that the amplitude and wavelengths of the unstable wave(s) be provided. In addition to this, this work simply assumed the existence of a finite amplitude state within the channel and did not examine the mechanism(s) leading to the wave's formation. The results of these efforts have been a very wide range of stability predictions which yielded poor comparisons with experimental results as demonstrated in the survey by Mata [14].

Experimental observation has lead to the belief that slugs form through either the evolution of short waves into large amplitude long waves or wave coalescence. These large amplitude wave-wave interactions cannot be captured by linear theory because it does not permit modal interactions. Experimental work was conducted by Jurman, Deutsch, and McCready [10] for the case of shear-generated interfacial waves in a cocurrent gas-liquid flow. This work provided spectral evolution of the interfacial waves and demonstrated that depending on the Reynolds number and void fraction, nonlinear energy transfer occurs among various interfacial modes by several possible mechanisms. Bi-coherence spectra were provided which demonstrated strong coupling between the various interacting modes.

The observations of energy transfer across the wave spectrum is similar to the effects observed in ocean wave environments. In 1960, Phillips [17] was the first to consider the effects of weak, nonlinear resonant wave-wave interactions in an ocean wave field. His work determined that these nonlinear interactions were responsible for transferring significant amounts of energy across the wavenumber spectrum and provided significant insight into the mechanics of the evolution surface-gravity waves.

Phillips' work, and a large number of follow up papers, such as Longuet-Higgins [13] works, apply a regular perturbation scheme to determine modal growth rates and quantify the rate of energy transfer. However, the time range over which this scheme is applicable is steepness limited. Subsequent work by McGoldrick [15] and Benney [3] applied the method of multiple scales to extend the theory of resonant wave-wave interactions by developing coupled nonlinear interaction equations for a discrete set of resonant wave modes. McGoldrick developed closed form, analytic solutions (taking on the form of Jacobian elliptic functions) which described the interfacial elevation of these discrete modes and demonstrated energy conservation (for non-dissipative conditions). Janssen [8], [9] considered the effects of resonant interactions between a primary mode and its second harmonic mode (referred to as a second harmonic resonance or an overtone resonance). His work found that this class of resonant interactions is responsible for the observed period doubling behavior seen in spectral measurements.

This multi-scale expansion was demonstrated to be accurate for times up to an order of magnitude longer than the traditional regular perturbation scheme. Since Phillips' 1960 paper, the theory of resonant wave-wave interactions among surface gravity waves has been a subject of active research and has reached maturity.

More recently, Bontozoglou and Hanratty [4] speculated that finite-amplitude Kelvin-Helmholtz waves undergo an internal second harmonic resonance which would result in the doubling of the wavelength of the unstable wave. It was believed that this could be part of the initial mechanism which would lead to the formation of slugs. However, at the time of publication, there was a lack of experimental evidence to support their conclusions.

In this work, the role that nonlinearity plays in the interfacial evolution of a two fluid stratified flow is examined. The nonlinear resonant wave-wave interactions which occur in KH stable flows are studied both analytically and numerically in order to calculate their growth rates and the rate of energy transfer. In addition to this, these resonant wave-wave interactions are examined for the case that the linear solution is unstable.

Since the majority of the slug stability models developed up to this point have been based on linear theories, this work provides insight into some of the physics which has been previously ignored. These methods are valid for steeper waves which are more representative of flows closer to the formation of liquid slugs.

Chapter 2

Theoretical Analysis

2.1 Fully Nonlinear Governing Equations

In this section, the fully nonlinear governing equations for a stratified flow through a horizontal channel are considered. The channel is divided into two separate domains corresponding to each of the two fluids. The coordinate system is located at the undisturbed interface between the two fluids with the x-coordinate extending horizontally to the right and the y-coordinate being directed vertically upwards. The vertical displacement of the interface away from its undisturbed position is defined by the function $y = \eta(x, t)$ and shall be described throughout the following analysis by both its frequency(ω) and wavenumber (k) spectra. The upper and lower fluids shall be denoted by the subscripts (u) and (l) respectively. The two fluids are of density ρ_u and ρ_l , where $\rho_u < \rho_l$, and have initial depths h_u and h_l . The viscosity in the upper and lower fluid shall be μ_u and μ_l respectively. Gravity and surface tension shall be denoted by g and γ .

The flow in each domain shall be decomposed into a constant uniform current and a disturbance flow. It is assumed that both of these flows are incompressible and irrotational such that the velocity of the fluids are defined by the gradient of their potential functions, $\Phi_u(x, y, t) = U_u x + \phi_u(x, y, t)$ and $\Phi_l(x, y, t) = U_l x + \phi_l(x, y, t)$,

which are governed within each domain by Laplace's equation:

$$\nabla^2 \Phi_u = \nabla^2 \phi_u = 0 \quad \eta < y < h_u \quad (2.1)$$

$$\nabla^2 \Phi_l = \nabla^2 \phi_l = 0 \quad -h_l < y < \eta \quad (2.2)$$

At the channel walls, the no penetration conditions are enforced such that:

$$\frac{\partial \phi_u}{\partial y} = 0 \quad y = h_u \quad (2.3)$$

$$\frac{\partial \phi_l}{\partial y} = 0 \quad y = -h_l \quad (2.4)$$

and the interface between the two fluids is material which requires that:

$$\frac{\partial \eta}{\partial t} + \left(U_u + \frac{\partial \phi_u}{\partial x} \right) \frac{\partial \eta}{\partial x} = \frac{\partial \phi_u}{\partial y} \quad y = \eta \quad (2.5)$$

$$\frac{\partial \eta}{\partial t} + \left(U_l + \frac{\partial \phi_l}{\partial x} \right) \frac{\partial \eta}{\partial x} = \frac{\partial \phi_l}{\partial y} \quad y = \eta \quad (2.6)$$

The dynamic boundary condition requires that the difference in the interfacial pressures, calculated by the Bernoulli equation, be balanced by the surface tension and the normal viscous stresses (described by Funada and Joseph [7]):

$$\begin{aligned} R \left[\frac{\partial \phi_u}{\partial t} + \frac{1}{2} \left(\frac{\partial \phi_u}{\partial x} \right)^2 + U_u \frac{\partial \phi_u}{\partial x} + \frac{1}{2} \left(\frac{\partial \phi_u}{\partial y} \right)^2 + \eta \right] \\ - \left[\frac{\partial \phi_l}{\partial t} + \frac{1}{2} \left(\frac{\partial \phi_l}{\partial x} \right)^2 + U_l \frac{\partial \phi_l}{\partial x} + \frac{1}{2} \left(\frac{\partial \phi_l}{\partial y} \right)^2 + \eta \right] \\ + \frac{2}{Re} \left[N \frac{\partial^2 \phi_u}{\partial y^2} - \frac{\partial^2 \phi_l}{\partial y^2} \right] = - \frac{1}{We} \frac{\eta_{xx}}{(1 + \eta_x^2)^{\frac{3}{2}}} + \frac{\hat{P}_f}{\rho_l g L} \quad y = \eta \quad (2.7) \end{aligned}$$

where $R = \frac{\rho_u}{\rho_l}$, $N = \frac{\mu_u}{\mu_l}$, $Re = \frac{\rho_l L \sqrt{Lg}}{\mu_l}$ and $We = \frac{L^2 g \rho_l}{\gamma}$. It should be noted that these

governing equations have been made non-dimensional with the normalization scheme:

$$\begin{aligned}
\left\langle \hat{x}, \hat{y}, \hat{\eta}, \hat{h}_u, \hat{h}_l, \frac{1}{\hat{k}} \right\rangle &= L \left\langle x, y, \eta, h_u, h_l, \frac{1}{k} \right\rangle \\
\left\langle \hat{\phi}_u, \hat{\phi}_l \right\rangle &= L \sqrt{Lg} \langle \phi_u, \phi_l \rangle \\
\left\langle \hat{U}_u, \hat{U}_l \right\rangle &= \sqrt{Lg} \langle U_u, U_l \rangle \\
\hat{t} &= \sqrt{\frac{L}{g}} t \\
\hat{P} &= \rho_l U^2 P = \rho_l L g P
\end{aligned} \tag{2.8}$$

where the $(\hat{\cdot})$ terms denoted dimensional quantities. Selection of the characteristic length (L) shall be described in Section 3.1 and the definition of the pressure forcing will be explained in Chapter 5.

2.2 Linear Solution

When Eqns. (2.1-2.7) are linearized about the mean interfacial elevation, the governing equations take on the form:

$$\nabla^2 \phi_u^{(1)} = 0 \quad 0 < y < h_u \quad (2.9)$$

$$\nabla^2 \phi_l^{(1)} = 0 \quad -h_l < y < 0 \quad (2.10)$$

$$\phi_{u,y}^{(1)} = 0 \quad y = h_u \quad (2.11)$$

$$\phi_{l,y}^{(1)} = 0 \quad y = -h_l \quad (2.12)$$

$$\eta_{,t}^{(1)} + U_u \eta_{,x}^{(1)} - \phi_{u,y}^{(1)} = 0 \quad y = 0 \quad (2.13)$$

$$\eta_{,t}^{(1)} + U_l \eta_{,x}^{(1)} - \phi_{l,y}^{(1)} = 0 \quad y = 0 \quad (2.14)$$

$$\begin{aligned}
R[\phi_{u,t}^{(1)} + U_u \phi_{u,x}^{(1)} + \eta^{(1)}] - [\phi_{l,t}^{(1)} + U_l \phi_{l,x}^{(1)} + \eta^{(1)}] \\
+ \frac{2}{Re} [N \phi_{u,yy}^{(1)} - \phi_{l,yy}^{(1)}] + \frac{1}{We} \eta_{,xx}^{(1)} = 0 \quad y = 0
\end{aligned} \tag{2.15}$$

The solution to this set of equations can be obtained by assuming a traveling wave solution for the interfacial elevation where upon substitution into the governing equa-

tions, the potential function coefficients can be found to take on the form:

$$\begin{aligned}
\eta^{(1)} &= -i\eta_o e^{i(kx-\omega t)} + c.c \\
\phi_u^{(1)} &= -\frac{(U_u k - \omega) \eta_o}{k \tanh(kh_u)} \frac{\cosh[k(y - h_u)]}{\cosh[kh_u]} e^{i(kx-\omega t)} + c.c \\
\phi_l^{(1)} &= \frac{(U_l k - \omega) \eta_o}{k \tanh(kh_l)} \frac{\cosh[k(y + h_l)]}{\cosh[kh_l]} e^{i(kx-\omega t)} + c.c
\end{aligned} \tag{2.16}$$

Substitution of this solution into the dynamic boundary condition yields the linear dispersion relationship:

$$\begin{aligned}
&\omega^2 \left[\frac{R}{k \tanh(kh_u)} + \frac{1}{k \tanh(kh_l)} \right] \\
&+ \omega \left[\frac{-2U_u R}{\tanh(kh_u)} + \frac{-2U_l}{\tanh(kh_l)} + \frac{2ik^2}{Re} \left(\frac{N}{k \tanh(kh_u)} + \frac{1}{k \tanh(kh_l)} \right) \right] \\
&+ \left[\frac{(U_l k)^2}{k \tanh(kh_l)} + \frac{R(U_u k)^2}{k \tanh(kh_u)} - \frac{2ik^2}{Re} \left(\frac{NU_u}{\tanh(kh_u)} + \frac{U_l}{\tanh(kh_l)} \right) \right. \\
&\quad \left. - (1 - R) - \frac{k^2}{We} \right] = 0 \tag{2.17}
\end{aligned}$$

Throughout the remainder of this document, the left-hand side of Eqn. (2.17) shall be denoted by $D(\omega, k)$. Under certain flow conditions, the dispersion relationship may yield complex frequencies of the form $\omega = \omega_R + i\omega_I$ for a given wave number (k). Given the form of the linear solution in Eqn. (2.16), it can be seen that for complex frequencies, the interfacial elevation shall grow exponentially with time which produces the classical Kelvin-Helmholtz (KH) instability. It is this behavior that has made this instability mechanism seem appropriate for predicting the transition from a stratified flow to slugs.

For a given set of flow parameters, the analytic dispersion relationship shows that the fastest instability occurs for short waves. However, experimental works, such as those by Jurman, Deutsch & McCready [10], have observed strong energy transfer from short to long waves. This characteristic behavior is impossible to see from linear theory because it does not permit modal interactions. This suggest that nonlinear interactions, which have been neglected from the majority of the previous studies,

will play a dominant role in the interfacial evolution and must be accounted for in stability predictions.

In addition to this, the linearization of the governing equations makes this theory only appropriate for disturbances of infinitesimal amplitude. While this linearized theory is acceptable for the initial interfacial development, there is a need for a more rigorous theory to be developed which can be capable of both promoting the growth of long waves and being able to make accurate predictions of finite-amplitude disturbances.

2.3 Weakly Nonlinear Formulation

In this section, the results of a weakly nonlinear analysis shall be considered in order to demonstrate the importance of the higher order effects on the interfacial dynamics. Initially, the linear solution shall be stable allowing for close form solutions to be derived. The case of a linearly unstable basic state shall be examined in Section 4.2. If it is assumed that ϕ_u , ϕ_l , and η are $O(\varepsilon) \ll 1$, where ε is a measure of the wave steepness, then these terms can be expanded in a regular perturbation series of the form:

$$\phi_u(x, y, t) = \sum_{m=1}^M \phi_u^{(m)}(x, y, t) \quad (2.18)$$

$$\phi_l(x, y, t) = \sum_{m=1}^M \phi_l^{(m)}(x, y, t) \quad (2.19)$$

$$\eta(x, t) = \sum_{m=1}^M \eta^{(m)}(x, t) \quad (2.20)$$

where $\phi_{u,l}^{(m)}$ and $\eta^{(m)}$ are $O(\varepsilon^m)$. Since determining the interfacial evolution is the primary objective of this work, it is necessary to calculate both of the potentials on the fluid interface. However, since this is a free boundary problem, with both $\phi_{(u,l)}$ and η being unknown functions, each potential can be expanded by means of a Taylor series such that it, and all of its derivatives, can be evaluated at $z = 0$ rather than

$z = \eta$ yielding an expression for the potentials of the form:

$$\phi(x, \eta, t) = \sum_{m=1}^M \phi^{(m)}(x, \eta, t) = \sum_{m=1}^M \sum_{k=0}^{M-m} \frac{\eta^k}{k!} \frac{\partial^k}{\partial y^k} \phi^{(m)}(x, y, t) \big|_{y=0} \quad (2.21)$$

It should be noted that the second summation is evaluated up to $M - m$ in order to maintain a consistent expansion up to $O(\varepsilon^M)$. When this perturbation expansion is applied to the fully nonlinear governing equations, higher order waves are found to exist which are coupled to the first order waves. For simplicity, the resulting derivation shall be limited to include up to second order effects ($M = 2$) yielding second order governing equations of the form:

$$\nabla^2 \phi_u^{(2)} = 0 \quad 0 < y < h_u \quad (2.22)$$

$$\nabla^2 \phi_l^{(2)} = 0 \quad -h_l < y < 0 \quad (2.23)$$

$$\phi_{u,y}^{(2)} = 0 \quad y = h_u \quad (2.24)$$

$$\phi_{l,y}^{(2)} = 0 \quad y = -h_l \quad (2.25)$$

$$\eta_{l,t}^{(2)} + U_u \eta_{u,x}^{(2)} - \phi_{u,y}^{(2)} = \phi_{u,yy}^{(1)} \eta^{(1)} - \eta_{l,x}^{(1)} \phi_{u,x}^{(1)} \quad y = 0 \quad (2.26)$$

$$\eta_{l,t}^{(2)} + U_l \eta_{l,x}^{(2)} - \phi_{l,y}^{(2)} = \phi_{l,yy}^{(1)} \eta^{(1)} - \eta_{l,x}^{(1)} \phi_{l,x}^{(1)} \quad y = 0 \quad (2.27)$$

$$\begin{aligned} R[\phi_{u,t}^{(2)} + U_u \phi_{u,x}^{(2)} + \eta^{(2)}] - [\phi_{l,t}^{(2)} + U_l \phi_{l,x}^{(2)} + \eta^{(2)}] + \frac{2}{Re} [N \phi_{u,yy}^{(2)} - \phi_{l,yy}^{(2)}] + \frac{1}{We} \eta_{,xx}^{(2)} = \\ \left[\eta^{(1)} \phi_{l,yt}^{(1)} + \frac{1}{2} \left(\phi_{l,y}^{(1)} \right)^2 + \frac{1}{2} \left(\phi_{l,x}^{(1)} \right)^2 + U_l \eta \phi_{l,xy}^{(1)} \right] - R \left[\eta^{(1)} \phi_{l,yt}^{(1)} + \frac{1}{2} \left(\phi_{l,y}^{(1)} \right)^2 + \frac{1}{2} \left(\phi_{l,x}^{(1)} \right)^2 + U_l \eta \phi_{l,xy}^{(1)} \right] \\ - \frac{2}{Re} [N \eta^{(1)} \phi_{u,yyy} - \eta^{(1)} \phi_{l,yyy}] \quad y = 0 \quad (2.28) \end{aligned}$$

If it is assumed that the first order interfacial solution is defined as:

$$\eta^{(1)} = a_1 \sin(k_1 x - \omega_1 t) + a_2 \sin(k_2 x - \omega_2 t) \quad (2.29)$$

then the second order interactions will create a solution with four additional wave

components and take on the general form:

$$\begin{aligned} \eta^{(2)} = & C_1 \sin(2k_1 x - 2\omega(k_1)t) + C_2 \sin(2k_2 x - 2\omega(k_2)t) \\ & + C_3 \sin(k_3 x - \omega_3 t) + C_4 \sin(k_4 x - \omega_4 t) \end{aligned} \quad (2.30)$$

where $k_3 = k_2 - k_1$, $k_4 = k_1 + k_2$, $\omega_3 = \omega(k_2) - \omega(k_1)$, and $\omega_4 = \omega(k_1) + \omega(k_2)$. It should be noted that additional nonlinear waves would be formed if either the order of nonlinearity (M) were increased or if the interface were composed of additional components. Upon solving the boundary value problem, the coefficients C_1 , C_2 , C_3 , and C_4 are found to take on the general form:

$$C_1 \sim \frac{A_1}{D(2\omega_1, 2k_1)} \quad C_2 \sim \frac{A_2}{D(2\omega_2, 2k_2)} \quad C_3 \sim \frac{A_3}{D(\omega_3, k_3)} \quad C_4 \sim \frac{A_4}{D(\omega_4, k_4)}$$

where A_j ($j = 1, \dots, 4$), are constants.

2.4 Regular Perturbation Solution for Nonlinear Resonant Wave-Wave Interactions

For most combinations of wave numbers and frequencies produced in the second order solution Eqn. (2.30), the dispersion relationship is not satisfied and the wave modes are independent. However, if the wave numbers and frequencies exactly satisfy the dispersion relationship, $D(\omega_j, k_j) = 0$, then that mode's amplitude becomes singular. This condition represents an interfacial resonance for which that second order wave component becomes coupled to the two first order modes. As a result, the amplitude of that second order mode grows at a rate which is proportional to time. The exact solution is found by assuming the following general form for the interfacial elevation

and potentials functions:

$$\eta^{(2)} = a_3 t e^{i(k_3 x - w_3 t)} \quad (2.31)$$

$$\phi_u^{(2)} = \left(A_3 t + \hat{A} \right) \frac{\cosh(k_3 [y - h_u])}{\cosh(k_3 h_u)} e^{i(k_3 x - w_3 t)} \quad (2.32)$$

$$\phi_l^{(2)} = \left(B_3 t + \hat{B} \right) \frac{\cosh(k_3 [y + h_L])}{\cosh(k_3 h_L)} e^{i(k_3 x - w_3 t)} \quad (2.33)$$

then by solving the boundary value problem, the amplitudes are found to be

$$\begin{aligned} a_3 &= \frac{R \mathbb{D}_u^{(3)} \tanh(k_3 h_l) P_1 + \mathbb{D}_l^{(3)} \tanh(k_3 h_u) P_2 + i k_3 \tanh(k_3 h_u) \tanh(k_3 h_l) P_3}{2 \left[R \tanh(k_3 h_l) \mathbb{D}_u^{(3)} + \tanh(k_3 h_u) \mathbb{D}_l^{(3)} \right]} \\ A_3 &= \frac{-i \mathbb{D}_u^{(3)} a_3}{k_3 \tanh(k_3 h_u)} \\ \hat{A} &= \frac{i \left(2 \mathbb{D}_l^{(3)} + R \frac{\tanh(k_3 h_l)}{\tanh(k_3 h_u)} \mathbb{D}_u^{(3)} \right) P_1 - i \mathbb{D}_l^{(3)} P_2 + k_3 \tanh(k_3 h_l) P_3}{2 i k_3 \left(R \tanh(k_3 h_l) \mathbb{D}_u^{(3)} + \tanh(k_3 h_u) \mathbb{D}_l^{(3)} \right)} \\ B_3 &= \frac{i \mathbb{D}_l^{(3)} a_3}{k_3 \tanh(k_3 h_l)} \\ \hat{B} &= \frac{i R \mathbb{D}_u^{(3)} P_1 - i \left(\frac{\tanh(k_3 h_u)}{\tanh(k_3 h_l)} \mathbb{D}_l^{(3)} + 2 R \mathbb{D}_u^{(3)} \right) P_2 - k_3 \tanh(k_3 h_u) P_3}{2 i k_3 \left(R \tanh(k_3 h_l) \mathbb{D}_u^{(3)} + \tanh(k_3 h_u) \mathbb{D}_l^{(3)} \right)} \end{aligned}$$

where

$$\begin{aligned} P_1 &= -i a_1^* a_2 k_3 \left[\mathbb{D}_u^{(1)} \coth(k_1 h_u) + \mathbb{D}_u^{(2)} \coth(k_2 h_u) \right] \\ P_2 &= i a_1^* a_2 k_3 \left[\mathbb{D}_l^{(1)} \coth(k_1 h_l) + \mathbb{D}_l^{(2)} \coth(k_2 h_l) \right] \\ P_3 &= a_1^* a_2 b_{12} \end{aligned}$$

with

$$\begin{aligned} \mathbb{D}_{u/l}^{(j)} &= U_{u/l} k_j - \omega_j \\ b_{12} &= \omega_1 \{ \mathbb{D}_l^{(1)} - R \mathbb{D}_u^{(1)} \} + \omega_2 \{ \mathbb{D}_l^{(2)} - R \mathbb{D}_u^{(2)} \} + \mathbb{D}_l^{(1)} \mathbb{D}_l^{(2)} (1 + \coth(k_1 h_l) \coth(k_2 h_l)) \\ &\quad - R \mathbb{D}_u^{(1)} \mathbb{D}_u^{(2)} (1 + \coth(k_1 h_u) \coth(k_2 h_u)) + k_1 \{ R U_u \mathbb{D}_u^{(1)} - U_l \mathbb{D}_l^{(1)} \} + k_2 \{ R U_u \mathbb{D}_u^{(2)} - U_l \mathbb{D}_l^{(2)} \} \end{aligned}$$

It is interesting to note that the second order potentials have non-zero amplitude at $t = 0$ when the interfacial amplitude is zero. This is the result of the linear solution creating a pressure field which requires that the second order solution have an initial velocity at $t = 0$. This finding is unique when compared to the solution obtained by Longuet-Higgins [13] for surface gravity waves where only one fluid was accounted for.

The magnitude of the initial amplitudes of the linear modes (k_1, k_2) are $O(\varepsilon)$ while the nonlinear resonant mode (k_3) mode is $O(\varepsilon^2)$. This regular perturbation expansion is valid for $|\eta^{(1)}| > |\eta^{(2)}|$. As the resonant mode grows, the expansion becomes invalid when $t \sim O(\varepsilon^{-1})$ because the magnitude of the second order mode is no longer in agreement with Eqn. (2.18 - 2.20). All other non-resonant modes were not considered because their amplitude remains $O(\varepsilon^2)$ for all time and would contribute little to the interfacial amplitude. In order to gain insight into the resonant growth for $t > O(\varepsilon^{-1})$ a different expansion procedure would need to be considered.

A special case of the triad resonance occurs between the k_1, k_1 and $2k_1$ modes. This second harmonic resonance has been documented by Janssen [8], [9] and Bontozoglou and Hanratty [4] and is believed to be present in evolution of the interface into slugs. This resonance condition occurs when

$$\omega(2k) = 2\omega(k) \tag{2.34}$$

It could also be considered as a requirement that the phase velocities of the primary mode and the second harmonic must equate. In traditional water wave mechanics, the second harmonic resonance is responsible for the transfer of energy between the second harmonic and the primary mode resulting in period doubling. It has been documented that the direction of energy transfer is periodic in time.

2.5 Multiple-Scale Analysis for Resonant Wave-Wave Interactions

In order to develop a solution to the long time evolution of the resonant growth, a perturbation expansion procedure must be employed which is valid for $t > O(\varepsilon^{-1})$. This can be done by calculating the second order solution utilizing the method of multiple scales.

Based on the regular perturbation expansion, resonance was observed at second order implying that the appropriate second time scale was $\tau = \varepsilon t$. The presence of a second time scale modifies the governing equations and requires that all time derivatives be replaced by

$$\frac{\partial[\]}{\partial t} \rightarrow \frac{\partial[\]}{\partial t} + \varepsilon \frac{\partial[\]}{\partial \tau}$$

The right hand side of Eqns. (2.26 - 2.27) has $-\eta_{,\tau}^{(1)}$ added to it. Similarly, $\phi_{l,\tau}^{(1)} - R\phi_{u,\tau}^{(1)}$ is added to the right hand side of Eqn. (2.28).

In this analysis, three modes of magnitude $O(\varepsilon)$ are assumed to exist at the interface and be of the form:

$$\eta^{(1)} = \sum_{j=1}^3 a_j(\tau) e^{i(k_j x - \omega_j t)} + c.c \quad (2.35)$$

$$\phi_u^{(1)} = \sum_{j=1}^3 A_j(\tau) \frac{\cosh(k_j[y - h_u])}{\cosh(k_j h_u)} e^{i(k_j x - \omega_j t)} + c.c \quad (2.36)$$

$$\phi_l^{(1)} = \sum_{j=1}^3 B_j(\tau) \frac{\cosh(k_j[y + h_u])}{\cosh(k_j h_l)} e^{i(k_j x - \omega_j t)} + c.c \quad (2.37)$$

where c.c denotes the complex conjugate and are subjected to the initial conditions $a_j(0) = \hat{a}_j$ (j=1,2,3). In this analysis, two of these modes shall represent the first order modes, while the third mode shall be the resonant mode that appeared at second order in the regular perturbation. However, since the method of multiple scales assumes that all three modes are of $O(\varepsilon)$, each mode must satisfy the linear

kinematic boundary conditions which prescribes the general form of the potential function amplitudes in terms of the interfacial amplitudes

$$A_j(\tau) = -\frac{i(U_u k_j - \omega_j)a_j}{k_j \tanh(k_j h_u)} \quad B_j(\tau) = \frac{i(U_l k_j - \omega_j)a_j}{k_j \tanh(k_j h_l)}$$

When the $O(\varepsilon)$ solution is used to calculate the forcing terms in Eqn. (2.26-2.28), terms arise which are in phase with the homogeneous solution. This produces the resonant condition:

$$\omega_2 - \omega_1 = \omega_3 + \sigma\varepsilon$$

where σ is a detuning parameter which is of $O(1)$ and allows for the modal responses away from exact resonances to be considered. These three boundary conditions combine to create the nonlinear interaction equations

$$\dot{a}_1 = a_2 a_3^* B_{23} e^{-i\sigma^* \tau} \quad (2.38)$$

$$\dot{a}_2 = a_1 a_3 B_{13} e^{i\sigma \tau} \quad (2.39)$$

$$\dot{a}_3 = a_1^* a_2 B_{12} e^{-i\sigma \tau} \quad (2.40)$$

with

$$B_{23} = \frac{iR\mathbb{D}_u^{(1)}C_u^{(1)}P_3 + i\mathbb{D}_l^{(1)}C_l^{(1)}d_3 - f_6k_1}{iR\mathbb{D}_u^{(1)}C_u^{(1)} + i\mathbb{D}_l^{(1)}C_l^{(1)} + f_1k_1} \quad (2.41)$$

$$B_{13} = \frac{iR\mathbb{D}_u^{(2)}C_u^{(2)}P_2 + i\mathbb{D}_l^{(2)}C_l^{(2)}d_2 - f_5k_2}{iR\mathbb{D}_u^{(2)}C_u^{(2)} + i\mathbb{D}_l^{(2)}C_l^{(2)} + f_2k_2} \quad (2.42)$$

$$B_{12} = \frac{iR\mathbb{D}_u^{(3)}C_u^{(3)}P_1 + i\mathbb{D}_l^{(3)}C_l^{(3)}d_1 - f_4k_3}{iR\mathbb{D}_u^{(3)}C_u^{(3)} + i\mathbb{D}_l^{(3)}C_l^{(3)} + f_3k_3} \quad (2.43)$$

where

$$P_1 = -ik_3 (\mathbb{D}_u^{(1)} \coth(k_1 h_u) + \mathbb{D}_u^{(2)} \coth(k_2 h_u))$$

$$P_2 = -ik_2 (\mathbb{D}_u^{(1)} \coth(k_1 h_u) + \mathbb{D}_u^{(3)} \coth(k_3 h_u))$$

$$P_3 = -ik_1 (\mathbb{D}_u^{(2)} \coth(k_1 h_u) + \mathbb{D}_u^{(3)} \coth(k_2 h_u))$$

$$\begin{aligned}
d_1 &= ik_3 \left(\mathbb{D}_l^{(1)} \coth(k_1 h_l) + \mathbb{D}_l^{(2)} \coth(k_2 h_l) \right) \\
d_2 &= ik_2 \left(\mathbb{D}_l^{(1)} \coth(k_1 h_l) + \mathbb{D}_l^{(3)} \coth(k_3 h_l) \right) \\
d_3 &= ik_1 \left(\mathbb{D}_l^{(2)} \coth(k_1 h_l) + \mathbb{D}_l^{(3)} \coth(k_2 h_l) \right)
\end{aligned}$$

$$\begin{aligned}
f_1 &= \frac{i}{k_1} \left(\mathbb{D}_l^{(1)} \coth(k_1 h_l) + R\mathbb{D}_u^{(1)} \coth(k_1 h_u) \right) \\
f_2 &= \frac{i}{k_2} \left(\mathbb{D}_u^{(2)} \coth(k_2 h_l) + R\mathbb{D}_u^{(2)} \coth(k_2 h_u) \right) \\
f_3 &= \frac{i}{k_3} \left(\mathbb{D}_l^{(3)} \coth(k_3 h_l) + R\mathbb{D}_u^{(3)} \coth(k_3 h_u) \right)
\end{aligned}$$

$$\begin{aligned}
f_4 &= \omega_1 \left(\mathbb{D}_l^{(1)} - R\mathbb{D}_u^{(1)} \right) + \omega_2 \left(\mathbb{D}_l^{(2)} - R\mathbb{D}_u^{(2)} \right) + k_1 \left(RU_u \mathbb{D}_u^{(1)} - U_l \mathbb{D}_l^{(1)} \right) + k_2 \left(RU_u \mathbb{D}_u^{(2)} - U_l \mathbb{D}_l^{(2)} \right) \\
&\quad + \mathbb{D}_l^{(1)} \mathbb{D}_l^{(2)} (1 + \coth(k_1 h_l) \coth(k_2 h_l)) - R\mathbb{D}_u^{(1)} \mathbb{D}_u^{(2)} (1 + \coth(k_1 h_u) \coth(k_2 h_u)) \\
f_5 &= \omega_1 \left(\mathbb{D}_l^{(1)} - R\mathbb{D}_u^{(1)} \right) + \omega_3 \left(\mathbb{D}_l^{(3)} - R\mathbb{D}_u^{(3)} \right) + k_1 \left(RU_u \mathbb{D}_u^{(1)} - U_l \mathbb{D}_l^{(1)} \right) + k_3 \left(RU_u \mathbb{D}_u^{(3)} - U_l \mathbb{D}_l^{(3)} \right) \\
&\quad - \mathbb{D}_l^{(1)} \mathbb{D}_l^{(3)} (1 - \coth(k_1 h_l) \coth(k_3 h_l)) + R\mathbb{D}_u^{(1)} \mathbb{D}_u^{(3)} (1 - \coth(k_1 h_u) \coth(k_3 h_u)) \\
f_6 &= \omega_2 \left(\mathbb{D}_l^{(2)} - R\mathbb{D}_u^{(2)} \right) + \omega_3 \left(\mathbb{D}_l^{(3)} - R\mathbb{D}_u^{(3)} \right) + k_2 \left(RU_u \mathbb{D}_u^{(2)} - U_l \mathbb{D}_l^{(2)} \right) + k_3 \left(RU_u \mathbb{D}_u^{(3)} - U_l \mathbb{D}_l^{(3)} \right) \\
&\quad + \mathbb{D}_l^{(2)} \mathbb{D}_l^{(3)} (1 + \coth(k_2 h_l) \coth(k_3 h_l)) - R\mathbb{D}_u^{(2)} \mathbb{D}_u^{(3)} (1 + \coth(k_2 h_u) \coth(k_3 h_u))
\end{aligned}$$

It should be noted that P_j , d_j , and f_j terms come from the right hand side of the upper kinematic, lower kinematic, and dynamic boundary conditions respectively. The Fredholm alternative, which takes on the form of Green's second identity, was applied to each of the potentials in order to guarantee uniqueness of the interaction equations.

It can be seen from Eqn. (2.38-2.40) that the Weber number does not appear explicitly in the interaction equations; however, the frequencies (ω_j) which are defined by the dispersion relationship are dependent on the Weber number. As a result, the role of surface tension is to adjust the dispersion curves and modify the resonance conditions.

2.5.1 Properties of Interaction Equations

The general solution to the interfacial amplitudes are in general complex functions. The decomposition scheme

$$a_j = r_j e^{i\theta_j} \quad (2.44)$$

with r and θ are real functions of the slow time variable (τ), can be applied to each of the modal amplitudes for the purpose of determining the slow time evolution of the amplitude and phase. This reduces Eqns. (2.38-2.40) the problem from three coupled complex differential equations to six real equations which take on the form:

$$\dot{r}_1 = -r_2 r_3 B_{23}^{(I)} \sin(\Gamma) \quad (2.45)$$

$$\dot{r}_2 = r_1 r_3 B_{13}^{(I)} \sin(\Gamma) \quad (2.46)$$

$$\dot{r}_3 = -r_1 r_2 B_{12}^{(I)} \sin(\Gamma) \quad (2.47)$$

$$r_1 \dot{\theta}_1 = r_2 r_3 B_{23}^{(I)} \cos(\Gamma) \quad (2.48)$$

$$r_2 \dot{\theta}_2 = r_1 r_3 B_{13}^{(I)} \cos(\Gamma) \quad (2.49)$$

$$r_3 \dot{\theta}_3 = r_1 r_2 B_{12}^{(I)} \cos(\Gamma) \quad (2.50)$$

where $\Gamma = \theta_2 - \theta_1 - \theta_3 + \sigma\tau$.

For an exact resonance $\sigma = 0$, the following property is valid

$$\frac{d}{d\tau} [r_1 r_2 r_3 \cos(\Gamma)] = 0$$

which requires that for $\Gamma = \pm\pi/2$ for all time. This conclusion that the relative phase (Γ) is constant for all τ then simplifies the governing equations from a set of six equations to a set of three interaction for the amplitudes

$$\dot{r}_1 = -r_2 r_3 B_{23}^{(I)} \quad (2.51)$$

$$\dot{r}_2 = r_1 r_3 B_{13}^{(I)} \quad (2.52)$$

$$\dot{r}_3 = -r_1 r_2 B_{12}^{(I)} \quad (2.53)$$

with $\theta_1 = \theta_1(0)$, $\theta_2 = \theta_2(0)$, and $\theta_3 = \theta_3(0)$.

In the following chapters, two cases will be considered through the use of numerical simulations. First, it will be demonstrated that in the event that a portion of the total wave number spectrum in a channel is unstable to the Kelvin-Helmholtz mechanism, while the remaining wave numbers are stable, nonlinear interactions and resonances can occur causing a rapid exchange of energy from the unstable short waves to the longer stable waves. Second, if the spectrum is stable to the KH mechanism, it is possible to achieve growth through energy transfer due to the turbulent pressure fluctuations in the gas stream. Nonlinear interactions will transfer energy to both shorter waves through higher harmonics and longer waves through nonlinear resonant interactions. In the following sections a numerical algorithm shall be described which shows the interfacial evolution of a wave number spectra and demonstrates that these resonances can exchange energy to wavelengths that are indicative of observed slug behavior.

Chapter 3

Numerical Simulation

3.1 Mathematical Formulation of a High Order Spectral Method

For this work, an efficient high order spectral (HOS) method, originally developed by Dommermuth and Yue [5] for the study of nonlinear surface gravity waves, was modified to simulate the nonlinear interfacial evolution of stratified channel flows. This method solves the primitive equations of the problem in the context of potential flow. The method follows the evolution of a large number of spectral interfacial wave modes and accounts for their interactions up to an arbitrarily high order of nonlinearity using a pseudo-spectral approach.

This process begins with the definition of the potentials at the interface within each fluid domain:

$$\phi_u^I(x, t) = \phi_u(x, \eta(x, t), t) \quad (3.1)$$

$$\phi_l^I(x, t) = \phi_l(x, \eta(x, t), t) \quad (3.2)$$

Applying chain rule to the interface potentials allows for the standard derivatives to

be written as:

$$\begin{aligned}\frac{\partial \phi^I}{\partial t} &= \frac{\partial \phi}{\partial t} + \frac{\partial \phi}{\partial y} \frac{\partial y}{\partial \eta} \frac{\partial \eta}{\partial t} \quad \Rightarrow \quad \frac{\partial \phi}{\partial t} = \frac{\partial \phi^I}{\partial t} - \frac{\partial \phi}{\partial y} \frac{\partial \eta}{\partial t} \quad @y = \eta \\ \frac{\partial \phi^I}{\partial x} &= \frac{\partial \phi}{\partial x} + \frac{\partial \phi}{\partial y} \frac{\partial y}{\partial \eta} \frac{\partial \eta}{\partial x} \quad \Rightarrow \quad \frac{\partial \phi}{\partial x} = \frac{\partial \phi^I}{\partial x} - \frac{\partial \phi}{\partial y} \frac{\partial \eta}{\partial x} \quad @y = \eta\end{aligned}$$

With these new definitions of the potential derivatives, the boundary conditions are written as functions of the interface potentials. The upper kinematic boundary condition takes on the form:

$$\frac{\partial \eta}{\partial t} = - \left[U_u + \frac{\partial \phi_u^I}{\partial x} \right] \frac{\partial \eta}{\partial x} + \left[1 + \left(\frac{\partial \eta}{\partial x} \right)^2 \right] \frac{\partial \phi_u}{\partial y} \quad @y = \eta \quad (3.3)$$

and by identical logic, the kinematic boundary condition for the lower fluid domain becomes:

$$\frac{\partial \eta}{\partial t} = - \left[U_l + \frac{\partial \phi_l^I}{\partial x} \right] \frac{\partial \eta}{\partial x} + \left[1 + \left(\frac{\partial \eta}{\partial x} \right)^2 \right] \frac{\partial \phi_l}{\partial y} \quad @y = \eta \quad (3.4)$$

Similarly, the dynamic boundary condition is modified to include the interface potentials:

$$\begin{aligned}\frac{\partial \psi_t^I}{\partial t} &= \frac{2}{Re} \left[N \frac{\partial^2 \phi_u}{\partial y^2} - \frac{\partial^2 \phi_l}{\partial y^2} \right] - (1-R)\eta + \frac{1}{2} \left[1 + \left(\frac{\partial \eta}{\partial x} \right)^2 \right] \left[\left(\frac{\partial \phi_l}{\partial y} \right)^2 - R \left(\frac{\partial \phi_u}{\partial y} \right)^2 \right] \\ &\quad + \frac{1}{2} \left[R \left(\frac{\partial \phi_u^I}{\partial x} \right)^2 - \left(\frac{\partial \phi_l^I}{\partial x} \right)^2 \right] + RU_u \frac{\partial \phi_u^I}{\partial x} - U_l \frac{\partial \phi_l^I}{\partial x} + \frac{1}{We} \frac{\eta_{xx}}{[1 + \eta_x^2]^{\frac{3}{2}}} \quad (3.5)\end{aligned}$$

where $\psi^I(x, t) \equiv \phi_l^I(x, t) - R\phi_u^I(x, t)$. Together, the kinematic and dynamic boundary conditions form a set of interfacial evolution equations that can be integrated in time to demonstrate the dynamic behavior of the interface between the two fluids.

If it is assumed that ϕ_u , ϕ_l , and η are $O(\varepsilon) \ll 1$, where ε is a measure of the wave steepness, then these terms can be expanded in a perturbation series up to order M

in terms of the small variable ε :

$$\phi_u(x, y, t) = \sum_{m=1}^M \phi_u^{(m)}(x, y, t) \quad (3.6)$$

$$\phi_l(x, y, t) = \sum_{m=1}^M \phi_l^{(m)}(x, y, t) \quad (3.7)$$

where $\phi^{(m)}$ is $O(\varepsilon^m)$. Since this is a free boundary problem, with both ϕ and η being unknown, each potential can be expanded by means of a Taylor series such that it, and all of its derivatives, can be evaluated at $y = 0$ rather than $y = \eta$

$$\phi(x, \eta, t) = \sum_{m=1}^M \phi^{(m)}(x, \eta, t) = \sum_{m=1}^M \sum_{k=0}^{M-m} \frac{\eta^k}{k!} \frac{\partial^k}{\partial y^k} \phi^{(m)}(x, y, t) \big|_{y=0} \quad (3.8)$$

It should be noted that the second summation is evaluated up to $M - m$ in order to maintain a consistent expansion up to $O(\varepsilon^M)$. Recalling that $\psi^I = \phi_l^I - R\phi_u^I$

$$\psi^I(x, \eta, t) = \sum_{m=1}^M \psi^{(m)}(x, \eta, t) = \sum_{m=1}^M \sum_{k=0}^{M-m} \frac{\eta^k}{k!} \frac{\partial^k}{\partial y^k} \psi^{(m)}(x, y, t) \big|_{y=0} \quad (3.9)$$

If all terms in this expansion of common order are collected, a set of Dirichlet boundary conditions for each $\psi^{(m)}(x, 0, t)$ can be defined as:

$$\psi^{(1)} = \psi^I \quad (3.10)$$

$$\psi^{(m)} = - \sum_{k=1}^{m-1} \frac{\eta^k}{k!} \frac{\partial^k}{\partial y^k} \psi^{(m-k)} \big|_{y=0} \quad (3.11)$$

where $\psi^I(x, t = 0)$ is provided as an initial condition.

Next, if the difference between the two kinematic boundary conditions, Eqn. (2.5 & 2.6), is taken, a new interfacial boundary condition can be made which takes on

the form:

$$\Phi_z = \eta_x (\Phi_x + [U_u - U_l]) \quad (3.12)$$

where $\Phi \equiv \phi_u - \phi_l$. By applying the perturbation expansions for Φ and then expanding in a Taylor series about $y = 0$ yields:

$$\Phi_u(x, \eta, t) = \sum_{m=1}^M \Phi_u^{(m)}(x, \eta, t) = \sum_{m=1}^M \sum_{k=0}^{M-m} \frac{\eta^k}{k!} \frac{\partial^k}{\partial y^k} \Phi^{(m)}(x, y, t) \big|_{y=0} \quad (3.13)$$

Using this expansion to calculate Φ_y , a set of Neumann boundary conditions can be written for each $\Phi_z^{(m)}$. Collecting all terms of common order yields:

$$\Phi_y^{(1)} = \eta_x [U_u - U_l] \quad (3.14)$$

$$\Phi_y^{(m)} = \eta_x \sum_{k=1}^{m-1} \frac{\eta^{(k-1)}}{(k-1)!} \frac{\partial^{(k-1)}}{\partial y^{(k-1)}} \Phi_x^{(m-k)} \big|_{y=0} - \sum_{k=1}^{m-1} \frac{\eta^k}{k!} \frac{\partial^{(k+1)}}{\partial y^{(k+1)}} \Phi^{(m-k)} \big|_{y=0} \quad (3.15)$$

These boundary value problems can be solved sequentially up to order M.

If it is assumed that the domain is to be 2π periodic in the x-direction, then the proper boundary value solutions, which satisfies both Laplace's equation and the no penetration conditions at the walls, can be written as a Fourier Series which takes take on the form:

$$\phi_u^{(m)}(x, y, t) = \sum_{n=-N}^N A_n^{(m)} \frac{\cosh(k_n [y - h_u])}{\cosh(k_n h_u)} e^{ik_n x} \quad (3.16)$$

$$\phi_l^{(m)}(x, y, t) = \sum_{n=-N}^N B_n^{(m)} \frac{\cosh(k_n [y + h_l])}{\cosh(k_n h_l)} e^{ik_n x} \quad (3.17)$$

The last remaining step is to determine the Fourier coefficients $A_n^{(m)}$ and $B_n^{(m)}$ of the

upper and lower potential functions. Recalling that $\psi^{(m)} = \phi_l^{(m)} - R\phi_u^{(m)}$:

$$\psi^{(m)} = \sum_{n=-N}^N \left(B_n^{(m)} \frac{\cosh(k_n[y + h_l])}{\cosh(k_n h_l)} - R A_n^{(m)} \frac{\cosh(k_n[y - h_u])}{\cosh(k_n h_u)} \right) e^{ik_n x} \quad (3.18)$$

where $\psi^{(m)}$ can also be expanded in a Fourier Series

$$\psi^{(m)} = \sum_{n=-N}^N \psi_n^{(m)} e^{ik_n x} \quad (3.19)$$

Equating terms of common wavenumber and evaluating at $y = 0$ yields:

$$\psi_n^{(m)} = B_n^{(m)} - R A_n^{(m)} \quad (3.20)$$

Similarly, using the definition $\Phi^{(m)} = \phi_u^{(m)} - \phi_l^{(m)}$:

$$\Phi^{(m)} = \sum_{n=-N}^N \left(A_n^{(m)} \frac{\cosh(k_n[y - h_u])}{\cosh(k_n h_u)} - B_n^{(m)} \frac{\cosh(k_n[y + h_l])}{\cosh(k_n h_l)} \right) e^{ik_n x} \quad (3.21)$$

and differentiating with respect to z :

$$\Phi_y^{(m)} = \sum_{n=-N}^N \left(A_n^{(m)} k_n \frac{\sinh(k_n[y - h_u])}{\cosh(k_n h_u)} - B_n^{(m)} k_n \frac{\sinh(k_n[y + h_l])}{\cosh(k_n h_l)} \right) e^{ik_n x} \quad (3.22)$$

Once again, expanding $\Phi_y^{(m)}$ in a Fourier series:

$$\Phi_y^{(m)} = \sum_{n=-N}^N \Phi_{n,y}^{(m)} e^{ik_n x} \quad (3.23)$$

and equating terms of common wavenumber and evaluating at $y = 0$:

$$\Phi_{n,y}^{(m)} = -k_n (A_n^{(m)} \tanh(k_n h_u) + B_n^{(m)} \tanh(k_n h_l)) \quad (3.24)$$

This leaves a set of equations that can be used to determine the coefficients of each

of the potential functions:

$$\psi_n^{(m)} = B_n^{(m)} - R A_n^{(m)} \quad (3.25)$$

$$\Phi_{n,y}^{(m)} = -k_n (A_n^{(m)} \tanh(k_n h_u) + B_n^{(m)} \tanh(k_n h_l)) \quad (3.26)$$

Algebraically solving this system yields the coefficients:

$$A_n^{(m)} = -\frac{\Phi_{n,y}^{(m)} + \psi_n^{(m)} k_n \tanh(k_n h_l)}{k_n (\tanh(k_n h_u) + R \tanh(k_n h_l))} \quad (3.27)$$

$$B_n^{(m)} = \frac{\psi_n^{(m)} k_n \tanh(k_n h_u) - R \Phi_{n,y}^{(m)}}{k_n (\tanh(k_n h_u) + R \tanh(k_n h_l))} \quad (3.28)$$

This leaves the potential functions in the upper and lower fluid fully specified throughout the entire domain and ready to be substituted into the two previously defined evolution equations Eqn. (3.3 & 3.5). Using a high order temporal integration scheme, such as the fourth order Runge-Kutta scheme, the free surface elevation (η) and the interface potential (ψ) can be integrated in time, once provided with an appropriate set of initial conditions.

It should be noted that the physical problem was always scaled such that the HOS simulations would be conducted on a computational domain of length 2π . For every trial, a physical domain length (L') would be supplied as input, and a normalized length scale could be defined as $L \equiv \frac{L'}{2\pi}$ where L is the variable used in Eqns. (2.8).

3.2 Validation of the Numerical Method

The numerical method was validated in several ways. The first test consisted of comparing the HOS simulations against the linear Kelvin-Helmholtz solution. Multiple simulations were carried out over a range of wavenumbers. For each test, the time

step or the grid density would be refined. The growth rates and frequencies were calculated from the numerical simulation and good agreement was observed with the analytical linear solution. The numerical solution was observed to converge exponentially fast with refinement of either grid or time step. The results of convergence tests have been tabulated and can be found in Tables A.1-A.4. In the following chapter, the numerical method shall also be compared against the nonlinear analytical solutions. Good agreement will also be observed thus validating the numerical method.

For the remainder of this paper, the order of nonlinearity is fixed to include up to second order effects since the focus is on understanding the importance of resonances on the interfacial evolution. At the initial time, a small artificial disturbance on the interface is created. By conducting numerical simulations, the nonlinear evolution of a particular set of wavenumber modes at the interface is identified and analyzed. From these simulations, insight is gained into the development of large amplitude disturbances through these nonlinear resonant wave-wave interactions.

Chapter 4

Kelvin-Helmholtz Flows

The aim of this chapter is to determine the affects of resonant wave-wave interactions in two-fluid channel flows. Initially, in Section 4.1, flow conditions are considered for which the frequency and wavenumber combinations are stable to the Kelvin-Helmholtz mechanism. The growth and modal interactions are examined using both the analytical and numerical methods developed in the previous chapters. The effects of near resonant wave interactions shall be considered.

Subsequent tests, in Section 4.2, consider flows where one or more of the resonant modes are linearly unstable to the Kelvin-Helmholtz mechanism. The resulting interactions and growth rates are documented and compared against the stable flow cases.

4.1 Kelvin-Helmholtz Stable Flows

The first set of tests examined frequency and wavenumber combinations which were stable to the Kelvin-Helmholtz mechanism. An air-water flow was considered with densities $\rho_u = 1.23 \frac{kg}{m^3}$ and $\rho_l = 999 \frac{kg}{m^3}$ respectively. The channel had a depth of 2.54 cm. and a void fraction of $\alpha \equiv \frac{h_u}{h_u + h_l} = 0.8$. For the initial set of results, the surface tension and normal viscous stresses are ignored. However, they are considered in Section 4.1.5. Since FFT's are utilized in the HOS method, it is necessary to ensure that all wavenumbers used by the method are integers. The physical domain length

was chosen to be $L' = 1\text{m}$ which sets the normalization length used by Eqn. 2.8 as $L = \frac{1}{2\pi}$. Gravity was taken to be $g = 9.81 \frac{\text{m}}{\text{s}^2}$.

A numerical algorithm was used to find the resonance conditions. For these stable flow trials, the dimensionless wavenumbers which satisfied triad resonance conditions were chosen to be $k_1 = 2$ and $k_2 = 98$. Based on the flow parameters identified in the preceding paragraph and $U_l = 0.002 \frac{\text{m}}{\text{s}}$, it was found that if the gas velocity was set to $U_u = 3.49935935513879 \frac{\text{m}}{\text{s}}$, the dispersion relationship would be satisfied to within $O(10^{-16})$. While this kind of accuracy is not possible for any experimental apparatus, this value was used for the initial numerical trials such that an "exact resonance" condition could be studied. Section 4.1.4 discusses how to relieve this strict tolerance by considering near resonance conditions allowing for more physically realizable trials to be examined. It should be noted that these particular sets of flow parameters were identified on the basis of demonstrating the relevant physical principals of interest, rather than corresponding to documented physical experiments from literature. Chapter 5 of this work shall make comparisons to available experimental data.

4.1.1 Comparison of Regular Perturbation to Multi-Scale Solution

Section (2.4) provided the regular perturbation solution for a triad resonant mode. The solution demonstrated that for initial time, the solution grew linearly with time as can be seen in Figure 4-1. However, this term is secular and as a consequence a_3/a_1 and a_3/a_2 grow without bounds as $t \rightarrow \infty$. Therefore the regular perturbation solution provides a correct prediction of the initial growth rate but is not uniformly valid for all time and breaks down when $\varepsilon t = O(1)$.

The multi-scale solution was derived for the sole purpose of being valid for times greater than $t > O(\varepsilon^{-1})$. The two time scales make this expansion procedure for $\varepsilon^2 t < O(1)$. A comparison between the regular perturbation solution and the multiple scale solution is shown in Figure 4-1 and demonstrates how the two solutions diverge

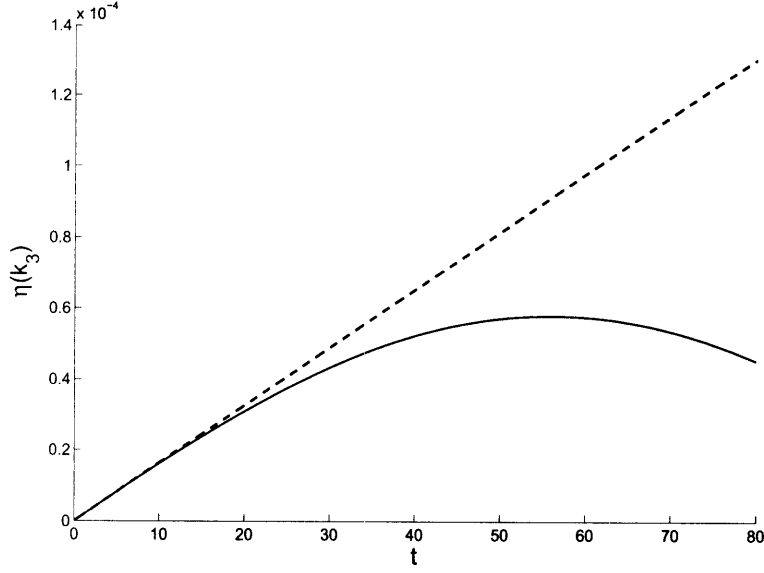


Figure 4-1: Comparison of the dimensionless amplitudes of the resonant mode determined by: regular(--) and multi-scale (—) perturbation method with the $\hat{a}_1(0) = \hat{a}_2(0) = 10^{-5}$ and $a_3(0) = 0$

with increasing time.

4.1.2 Effect of Wave Steepness

The validity of the multi-scale solution was tested, by comparing the analytical solutions with the numerical solutions produced by the HOS method. Several simulations were conducted over a range of initial wave amplitudes/steepnesses and their comparisons are shown in Figure 4-2.

Generally, good agreement is observed between the multi-scale and the HOS method solutions. For small initial amplitudes of $O(10^{-6} - 10^{-5})$, the multi-scale solution and the numerical results are nearly indistinguishable from one another. This close correspondence is maintained for many periods of the slow time scale. As the initial amplitudes are increased and approach $O(10^{-4})$, a small difference between the two solutions is observable. The maximum amplitude of the HOS solution appears to become smaller than the multi-scale solution and a small phase shift between the two solutions develops. These effects become more prominent and the two solutions

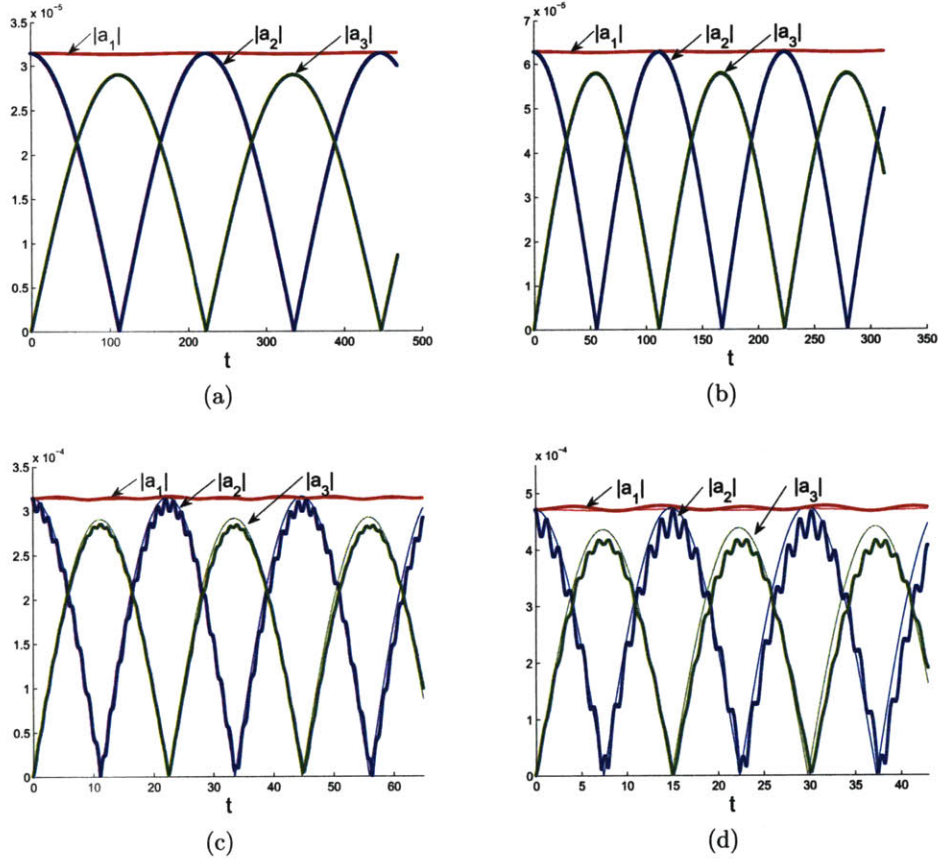


Figure 4-2: Validation of nondimensional modal amplitudes calculated by (-) multi-scale solution and (-) numerical method for $\hat{a}_1(0) = \hat{a}_2(0) = \hat{\eta}_0$ where in: (a) $\hat{\eta}_0 = 5 \times 10^{-6}\text{m}$, (b) $\hat{\eta}_0 = 1 \times 10^{-5}\text{m}$, (c) $\hat{\eta}_0 = 5 \times 10^{-5}\text{m}$, (d) $\hat{\eta}_0 = 7.5 \times 10^{-5}\text{m}$

slowly diverge as the wave steepness is increased or as t becomes large.

The results of Figure 4-2 show that regardless of the initial amplitude, the resonant mode (a_3) always rises to approximately 92% of the initial amplitude of the other two resonant modes (a_1, a_2). The amplitudes of a_2 and a_3 appear to be completely out of phase since when a_3 reaches it's maximum, $a_2 \rightarrow 0$. As the waves become steeper, the interaction periods decrease significantly. The rise time of the resonant mode (the time required for a_3 to go from zero to its first maxima) appears to decrease nearly exponentially with increasing initial amplitude of the two primary modes.

The magnitude of a_1 remains approximately constant throughout the duration

of the interactions. As the initial conditions become steeper, the magnitude of the oscillations become more apparent; however, these fluctuations are insignificant in comparison to a_2 and a_3 . It can be observed from Figure 4-2d that a_1 is approximately a quarter period out of phase with a_2 and a_3 . Similar behavior was observed by McGoldrick [15] in the multiscale solution for single fluid water waves of infinite depth.

4.1.3 Verification of Special Properties

Section 2.5.1 analytically proved that when the exact resonance conditions are satisfied, the relative phase between the three resonant modes $\Gamma = \theta_2 - \theta_1 - \theta_3 = \pm\pi/2$ and remains constant for all time. This can easily be demonstrated numerically by applying the same decomposition scheme, Eqn. (2.44), to the HOS solution. The resulting time evolution of the amplitudes and phases of the resonant modes, with the initial amplitudes of $\hat{a}_1(0) = \hat{a}_2(0) = 5 \times 10^{-5}$ and $a_3(0) = 0$ is shown in Figure 4-3.

It should be noted that this resonance condition ($\Gamma = \pm\pi/2$) can either be exposed as $a_j > 0$ while $0 \leq \theta_j < 2\pi$ or as $a_j \in \mathbb{R}$ while $\Gamma = -\pi/2$ or $\pi/2$. Figure 4-3 shows the latter case. This validates the theoretical conclusion, derived in Section 2.5.1, and demonstrates that the relative phase between the resonant triads is constant for the case of an exact resonance condition.

4.1.4 Near Resonant Interactions

The findings shown up to this point have been for exact resonance conditions for which the dispersion relationship was satisfied to $O(10^{-16})$. The accuracy required to achieve this condition is very strict and could not be achieved by any known experimental apparatus; however, large amplitude motion of the k_3 -mode is still achievable for conditions near the exact resonance. The original amplitude equations Eqns. (2.38-2.40), derived in Section 2.5, account for these affects by including a detuning parameter σ (which until now has been zero). The affect of near resonance conditions

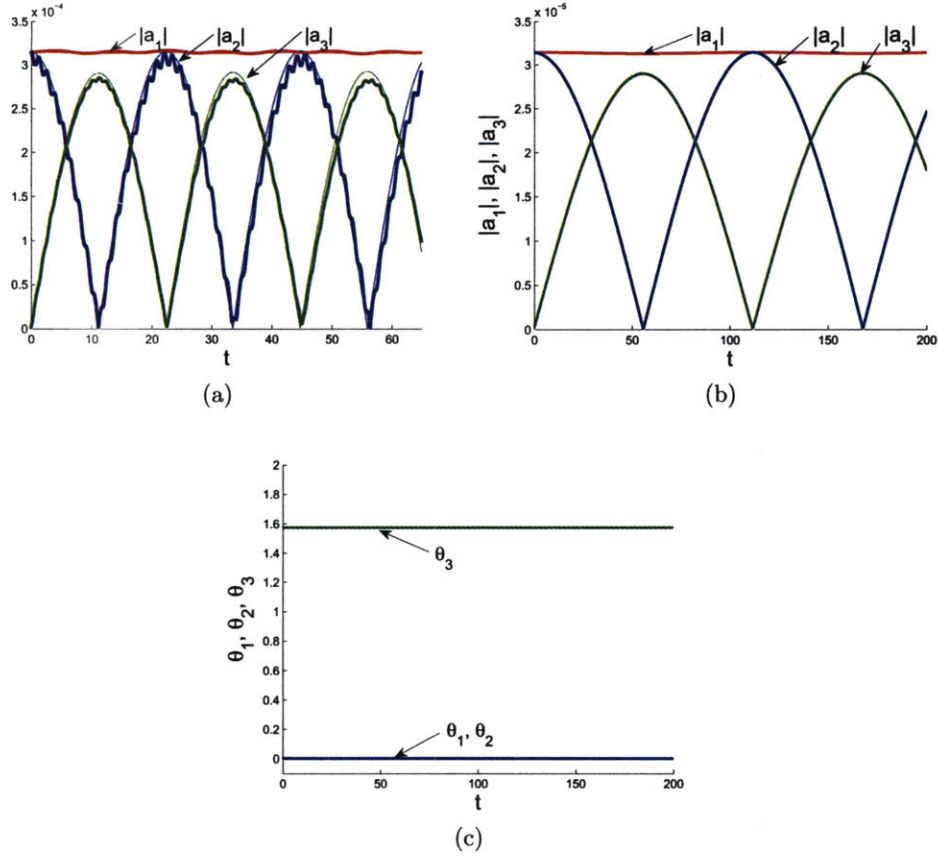


Figure 4-3: Validation of constant relative phases between the resonant modes where (a) is the exact numerical solution, (b) the magnitude of the amplitudes, and (c) shows the phases of each of the modes

can be observed by considering several simulations over a range of σ . The resulting simulations are shown in Figure 4-4

Figure 4-4a compares the difference between the exact resonance case (represented by the thin lines) and the near resonance case (represented by the thick lines). For this test, the upper gas velocity was changed from $U_u = 3.49935935513879 \frac{m}{s}$ to $U_u = 3.48 \frac{m}{s}$ resulting in a detuning factor of magnitude $\varepsilon\sigma = 0.033123$. The results of Figure 4-4a demonstrates that as the flow conditions are adjusted to be slightly away from the exact resonance condition, the amplitude of the resonant (a_3) begins to decrease as does the slow time period of oscillation. More specifically, the amplitude

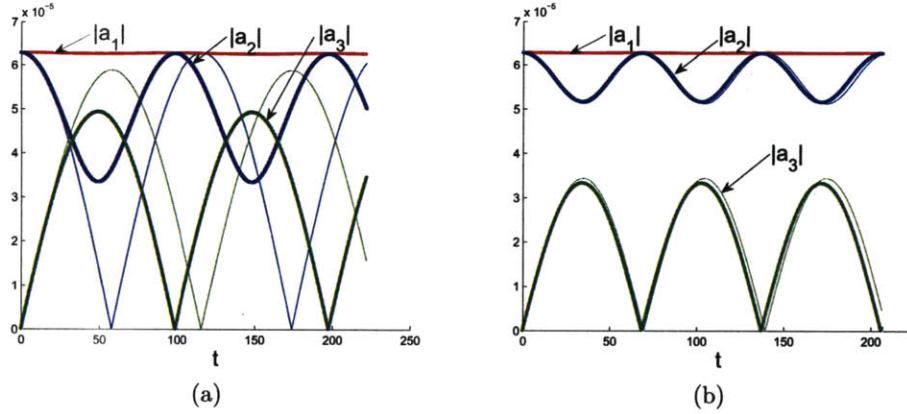


Figure 4-4: Effect of the detuning parameter on near resonant interactions. Case (a) comparison between (—) "exact resonance" and (---) near resonance for $U_u = 3.48 \frac{m}{s}$ with ($\varepsilon\sigma \approx 0.0331232$), (b) Comparison between (—) HOS solution and (---) multi-scale solution for the near resonance solution with larger detuning ($\varepsilon\sigma = 0.07335$) for $U_u = 3.45 \frac{m}{s}$.

of the resonant mode (a_3) decreases by 15.7% and the slow-time period of oscillation decreased by 14.8% from the exact resonance case. So, despite not exactly satisfying the linear dispersion relationship, large amplitude response is still achievable from near resonant interactions.

When the three modes exactly satisfy the dispersion relationship, the a_2 approaches zero as the a_3 approaches its maximum. For the near resonant interaction case, the minimum of a_2 is nonzero and occurs 15.3% sooner than the exact resonance case. More generally, the a_2 component remains of non-zero amplitude for the entirety of the interaction period. Throughout the course of these interactions, the response of a_1 remained approximately constant irrespective of whether the interactions satisfy an exact or near resonance condition. Small amplitude oscillations are observed; however the magnitude is insignificant in comparison to the magnitude of a_2 and a_3 .

If the flow conditions are adjusted to be further away from the exact resonant conditions, the trends previously observed are still valid, as observed in Figure 4-5a. In this case, the upper gas velocity was set to $U_u = 3.45 \frac{m}{s}$ resulting in a detuning parameter of magnitude $\varepsilon\sigma = 0.073349$. The value of the detuning parameter has

increased by approximately 55% from the previous trial shown in Figure 4-4a. The amplitude of a_3 decreased by 41.2% while the slow-time period decreased by 39.5% from the exact resonance case. Similarly, the minimum value of a_2 remains non-zero, and is of larger amplitude than in the previous near resonance condition. The first minimum of a_2 occurs 40.15% faster than the exact resonance case. The trends observed are universal and become more prominent as the detuning parameter $\varepsilon\sigma$ increases.

4.1.5 Effect of Surface Tension and Normal Viscous Stresses

As noted in Section 2.5, the only effect of surface tension was to adjust the shape of the dispersion relationship. For certain values of the Weber number, it may be possible to see multiple resonances for a certain set of wavenumbers.

A numerical trial was conducted for an air-water flow with upper and lower fluid velocities of $U_u = 3.48 \frac{m}{s}$ and $U_l = 0.002 \frac{m}{s}$. The viscosities used for the two fluids were $\mu_u = 10^{-3} \frac{N-s}{m^2}$ and $\mu_l = 1.8 \times 10^{-5} \frac{N-s}{m^2}$. When the dispersion relationship was analyzed, a triad resonance was found to exist between $k_1 = 1$, $k_2 = 60$, and $k_3 = 59$. Surface tension was included and had a coefficient $\gamma = 7.34 \times 10^{-2} \frac{N}{m}$.

When the normal viscous stresses are included, the energy of the previously stable triad is no longer conservative. Over many periods of oscillations, all three wave modes are damped back to the stable undisturbed interfacial configuration. These viscous effects have been incorporated into the HOS method and are shown in Figure 4-5.

While the viscous effects are removing energy from the system, Figure 4-5 shows that the k_3 -mode can still reach a finite-amplitude state. However, the long term periodic structure that was previously observed is no longer apparent because both the k_2 - and k_3 -modes decay rapidly back to the undisturbed state. The k_1 -mode remains approximately constant over the course of the interactions because $\omega_I(k_1) \approx 0$. The damping effect on the long wave mode would become more prominent over a much longer observation period.

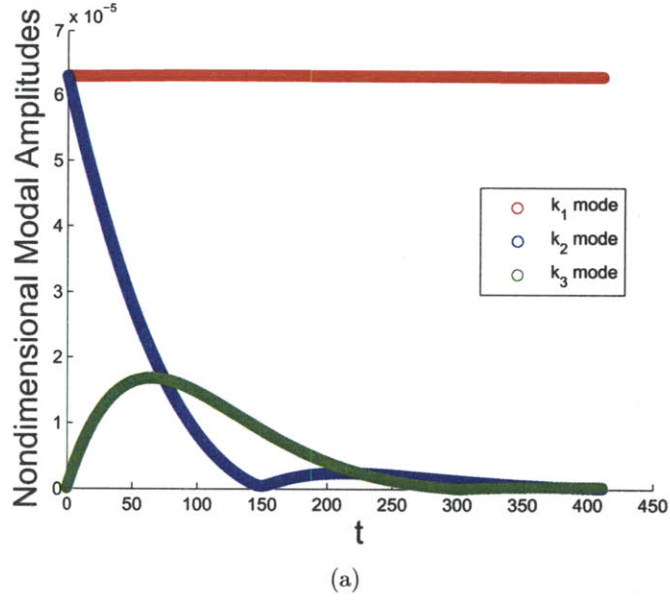


Figure 4-5: Effect of the normal viscous stresses on triad interactions for air water flow with $\mu_u = 10^{-3} \frac{N-s}{m^2}$, $\mu_l = 1.8 \times 10^{-5} \frac{N-s}{m^2}$ and $k_1 = 1$, $k_2 = 60$, and $k_3 = 59$

4.2 Kelvin-Helmholtz Unstable Flows

In this section, resonant wave-wave interactions are considered for which one or more of the interacting modes is linearly unstable due to the Kelvin-Helmholtz mechanism. The first case to be considered is the interaction of two stable modes and one linearly unstable mode. It will be shown that it is possible for all three interacting modes to grow simultaneously to finite-amplitudes. The second harmonic resonance will also be demonstrated and similar results shall be observed. The final result to be demonstrated shall examine the effects of combined resonances. In these interactions, a triad resonance was considered with two modes near the neutral point (one of which is linearly unstable) and have a difference component which creates a long wave. Simultaneously, the unstable wave from the triad resonance shall also be in a near second harmonic resonance. It will be observed that unstable energy can be transferred across the wave spectra and create large amplitude growth of the long wave components.

For all of the tests, the same flow geometry as in the previous section shall be

considered. The channel was 2.54 cm. deep with a void fraction of $\alpha = 0.8$. Surface tension was $\gamma = 0.0734 \frac{N}{m}$ and gravity was $g = 9.81 \frac{m}{s^2}$. The lower gas velocity shall be $U_l = 0.00215 \frac{m}{s}$, and the upper gas velocity shall be $U_u = 12 \frac{m}{s}$. This gas velocity was selected such that the dispersion curve would admit a sufficient number of wave modes which were unstable to the Kelvin-Helmholtz mechanism. The physical domain was chosen to be one meter yielding the same characteristic length scale as in the previous case. Initially the interface shall be composed of a set of two linear wave-modes of wavenumber k_1 and k_2 respectively with initial amplitudes of 10^{-5} .

The multi-scale method was found to be inappropriate for flows containing linearly unstable modes. When the multi-scale solution was derived in a manner similar to that of Section 2.5 the interaction equations were found to contain both fast and slow time scales, thus violating the assumptions built into the multi-scale method. Previous attempts have been made to overcome this but required the instability to be weak and was valid only for small interaction times. In the cases considered in section, the instability is not weak. As a result, HOS method was used instead to simulate the interfacial evolution.

4.2.1 Triad Resonance

The first case considered was for a wavenumber set where k_1 is stable and k_2 was an unstable wavemode near the neutral point of the dispersion curve. The difference component (k_3) was stable to the KH mechanism. It should be noted that for interactions where one of the modes is linearly unstable, only near resonant interactions are possible. The current set of wave modes have frequencies of the form $\omega_1 = \omega_1^{(R)}$ and $\omega_2 = \omega_2^{(R)} + i\omega_2^{(I)}$ with the difference frequency $\omega_3 = \omega_3^{(R)} = \omega_2^{(R)} + i\omega_2^{(I)} - \omega_1^{(R)}$. The ω_2 component has an unbalanced imaginary part making it impossible for this equality to ever be satisfied. Therefore, this triad set can only be near resonance.

For the first trial, the stable and unstable wavenumbers were $k_1 = 4$ and $k_2 = 5$ respectively. The k_2 mode was the first unstable wavenumber in the spectra which was an integer wavenumber (the HOS method can only simulate integer wavenumbers). The resulting interfacial evolution can be seen in Figure 4-6.

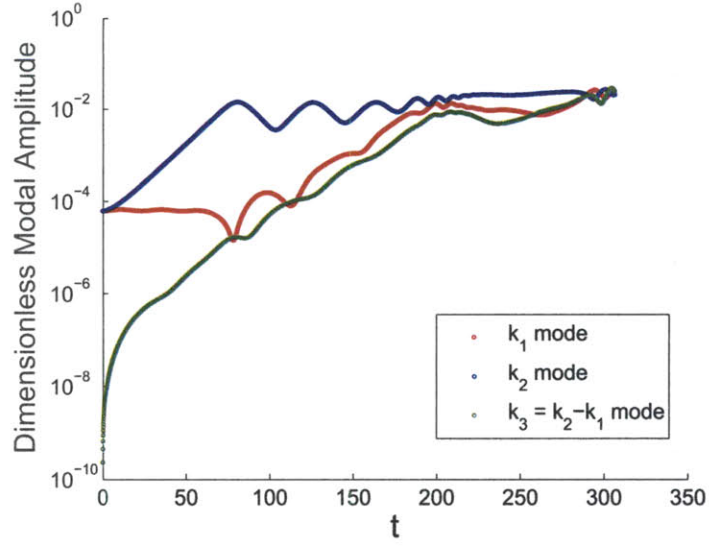


Figure 4-6: Unstable Triad Resonance with k_1 and k_3 stable and k_2 being unstable to the KH mechanism

This figure demonstrates that initially the k_1 mode is stable since until $t \sim 50$, the amplitude remains nearly constant with only very small amplitude oscillations arising from the second order resonant interactions. The k_2 -mode grows exponentially with time as predicted by the linear KH theory, until nonlinearity bounds it and stops the exponential growth its growth around $t \sim 75$. By the time the k_2 mode stops growing exponentially, the amplitude of the k_3 mode increased to $O(10^{-5})$.

At this time, the three modes begin interacting strongly together. The k_1 - and k_3 -modes continue to grow until their amplitudes are of the same order as the linearly unstable k_2 mode, $O(10^{-2})$. This feature is unique for several reasons. Typically the three interacting modes do not all grow simultaneously. To the author's knowledge, that has only been observed under the very special conditions of the explosive instabilities. In addition to this, for the stable resonances, the k_3 -mode was only observed to grow to a maximum amplitude which was of the order of the of the initial amplitudes of the other two resonating modes, $O(10^{-5})$ for this system. For this system, with the linearly unstable mode, the k_3 mode grew an extra three orders of magnitude above the initial conditions of the system. The periodic structure seen in the stable

resonance is no longer present.

It would seem that the linearly unstable k_2 becomes a source in the triad resonant interactions and continuously supplies energy to the triad of wave modes. Over the course of the interactions, all modes grow to substantially larger amplitude than would ever be seen by the standard stable resonant interactions.

The fact that the k_3 -mode grows to such large amplitudes is substantial because typically, all of the existing theories that try to predict the generation of slugs rely on linear wave theories based on modified Kelvin-Helmholtz mechanisms. Those theories would suggest that all wave-numbers less than k_1 would be stable and never grow; however, this resonance mechanism has demonstrated that is most certainly not the case and can in fact grow to similar amplitudes as large as any linearly unstable modes.

4.2.2 Second Harmonic Resonance For Unstable Flows

For this trial, the near second harmonic resonance is considered. The interface is initialized with a single mode near the neutral point of the dispersion curve. When this linear mode satisfies the second harmonic resonance condition, rapid energy can be exchanged between the two modes. Two cases are considered. The first has the linear mode being unstable but close to the neutral point, while in the second case the mode is the neutral point. The resulting interfacial evolution of these two trials is shown in Figure 4-7.

The first trial, shown in Figure 4-7a has the linear mode ($k_1 = 5$) being unstable, but near the neutral point. This mode was considered first because it was the closest integer wavenumber to satisfying the second harmonic resonance conditions. It can be seen in Figure 4-7a that for small time, both modes grow exponentially with time; however, the $2k_1$ -mode has a significantly larger growth rate than the linear mode. Around $t \sim 10$, the second order nonlinearity prevents the $2k_1$ mode from growing exponentially with time and bounds its growth. This mode begins oscillating and rings down to an asymptotic value of $O(10^{-2})$. While this ring down occurs, the k_1 -mode is still growing due to the energy transfer from the resonant interactions;

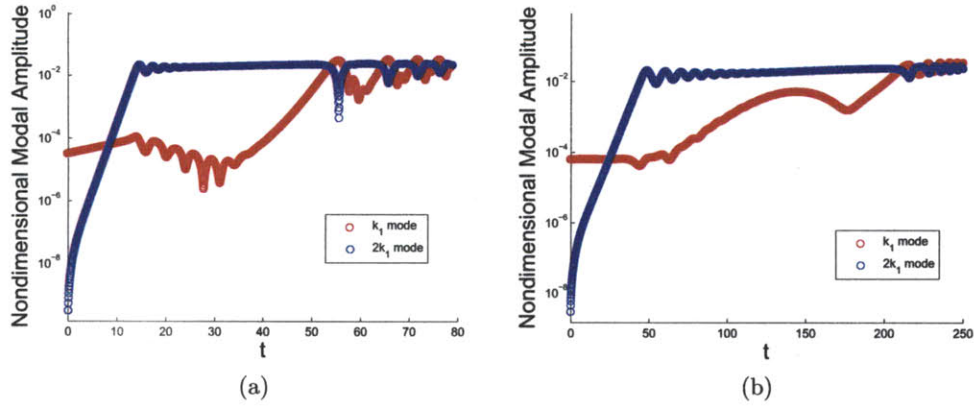


Figure 4-7: Effect of second harmonic resonance with $2k_1$ component being linearly unstable. In these trials k_1 -mode is (a) linearly unstable (b) linearly stable to the KH mechanism

however, around $t \sim 50$ the k_1 -mode reaches its limit, the k_1 - and $2k_1$ modes begin interacting as is typically observed in the classical stable second harmonic resonance. Figure 4-8 shows these interactions on a linear scale. A unique feature that can be observed is that these interactions is that they are no longer the smooth type of oscillations that would be observed from Jacobian elliptic functions. Extra humps are observed around the minima of the k_1 -mode and the maxima of the $2k_1$ -mode.

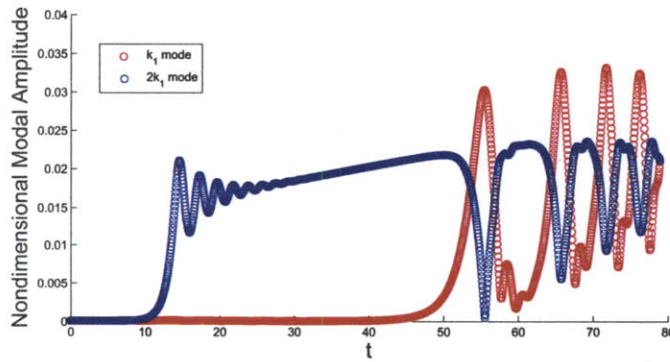


Figure 4-8: Time trace of the second harmonic resonance with both k_1 and $2k_1$ being linearly unstable to KH

Figure 4-7b shows the case where k_1 is linearly stable. As in the previous case, the $2k_1$ -mode grows exponentially with time as expected by the KH instability. Once

it reaches a limiting steepness, the exponential growth phase stops and the amplitude rings down to an asymptotic value of similar order as is observed in Figure 4-7a. However, since the k_1 -mode is stable, there is less energy involved in the second harmonic interaction. As a result, the growth rate is slower and nonlinearly doesn't bound the $2k_1$ component until $t \sim 40$. Despite the weaker interactions in comparison to the previous trial, the resonant interactions still cause the k_1 mode to grow until it is of similar order as the $2k_2$ -mode. Once the magnitude of $a(k_1)$ and $a(k_2)$ are of similar order, the two components begin to interact in a similar fashion to the previous trial, but with significantly smaller amplitude.

As in the triad resonance case, it is interesting to observe that the strong resonant interactions occur after both modes have stopped their exponential growth phase, yielding oscillations which are of significantly larger amplitude than was observed in the stable resonance cases.

4.2.3 Combined Triad and Second Harmonic Resonance

In this final section, the more complicated case shall be considered which allows for both the triad and second harmonic resonant interactions to occur simultaneously. This is possible when there is a second harmonic resonance between a wave-mode near the neutral point and its second harmonic as well as a triad resonance between that same wave-mode near the neutral point, and two other wave-modes in the stable region of the dispersion curve.

Figure 4-9a shows the basis trial for which there is only a near triad resonance between k_1 , k_2 , and $k_3 = k_2 - k_1$, with the k_2 mode being linearly unstable. This is exactly the same trial that was examined in Section 4.2.1. From this figure it can be seen that all three modes become $O(10^{-2})$ when $t \sim O(300)$. This resonance is very slow growing but creates large amplitude growth of the long wave components.

When a fourth mode is allowed to interact with the triad, the dynamics change and can result in accelerated growth of long waves. Figure 4-9b shows the evolution when the k_2 and $2k_2$ components were in a near second harmonic resonance. Simultaneously, there was also a near triad resonance between k_1 , k_2 , and k_3 with k_2 being

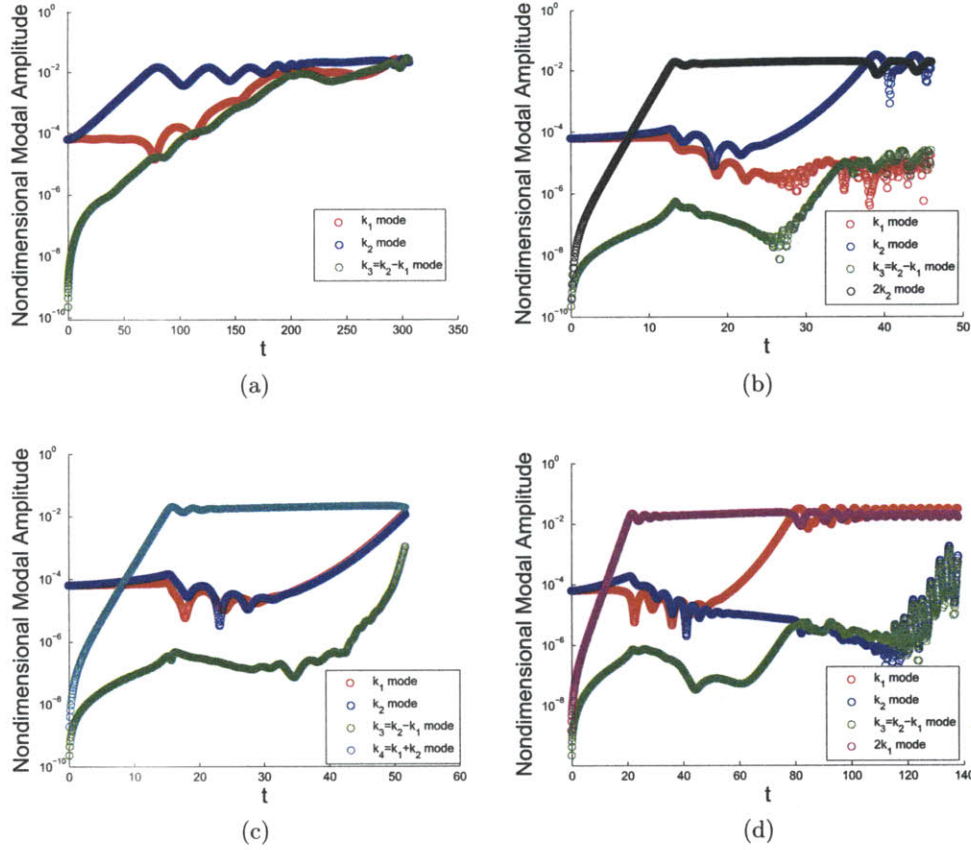


Figure 4-9: Combined triad and (a) only the original triad components, (b) sum-mode ($k_1 + k_2$), (c) k_1 -mode's second harmonic ($2k_1$), (d) k_2 -mode's second harmonic ($2k_2$)

linearly unstable. This figure shows that the k_2 -mode and the $2k_2$ -mode grow exponentially with time, as is expected from the Kelvin-Helmholtz mechanism. The $2k_2$ mode grows much more rapidly because its growth rate is significantly larger than k_2 . Around $t \approx 12$, the nonlinearity stops the $2k_2$ from growing exponentially, and it appears to approach an asymptotic value. Only small oscillations appear which are most likely due to the weak interactions of the second harmonic resonance. Simultaneously, the long k_3 component grew to an amplitude of $O(10^{-6})$. It temporarily stopped growing at approximately the same time as the $2k_2$ component stopped growing exponentially. The k_1 , k_2 , and k_3 modes oscillate due to the near triad resonance, while simultaneously, the k_2 mode grows due to the second harmonic resonant inter-

actions with $2k_2$. All of the wave modes continue to grow simultaneously. In this trial, the short waves became steep and began to break which caused the simulation to stop.

It should be noted that the exact resonance condition is located between the $\{k_1, 2k_1\}$ and $\{k_2, 2k_2\}$ near resonances on the dispersion curve. As a result, strong near resonant interactions can also occur by including the sum mode $k_1 + k_2$ and the $2k_1$ modes to interact with the two primary modes. These cases be observed in Figures 4-9c and 4-9d. Figure 4-9c, which shows the affect of the sum mode, shows similar trends as observed in Figure 4-9b, except in this case even stronger growth of the k_3 -mode can be observed causing it to rapidly approach $O(10^{-2})$. This rapid growth occurs in approximately the same time as in the previous trial.

Figure 4-9d, which shows the affect of the $2k_1$ -mode, demonstrates similar results as the previous two trials, but in this case, the rise times are significantly slower. Large amplitude growth of the a_3 -mode is still observed, but it takes 280% longer than the previous two trials. This signifies that this near resonance between the primary modes and the $2k_1$ mode is the weakest out of these three cases examined.

When the problem is generalized to include all second order interactions, $k_2 - k_1$, $2k_1$, $k_1 + k_2$, and $2k_2$, the behavior observed before becomes even more obvious as shown in Figure 4-10. For this trial, k_2 , $2k_1$, $k_1 + k_2$, and $2k_2$ are all linearly unstable and grow exponentially with time. Since $2k_1$, $k_1 + k_2$, and $2k_2$ all have similar growth rates, they all become bounded by nonlinearity at approximately the same time ($t \sim 12$). At this time, strong second harmonic resonances occur resulting in significant amounts of energy to be transferred from the unstable wave components to the primary wave modes(k_1, k_2). Simultaneously, these two primary modes are involved in a triad resonance with the difference component (k_3) causing it to grow from zero to $\approx O(10^{-3})$. This continued unstable growth causes significant amounts of energy to be transferred across the spectra allowing k_3 to reach magnitudes of $O(10^{-2})$.

This resonant mechanism can be summarized by the energy flow map depicted by Figure 4-11. This figure depicts the case of a second harmonic resonance between

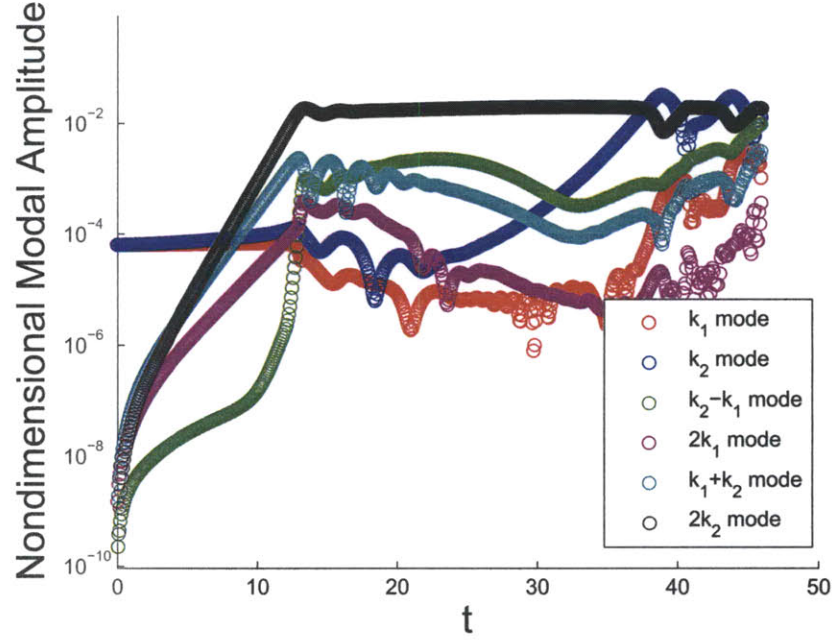


Figure 4-10: Combined resonance in which all second order components $k_1, k_2, 2k_1, k_1 + k_2, 2k_2$ are included

the $\{k_2, 2k_2\}$ and a triad resonance between $\{k_1, k_2, k_3\}$. Energy is generated by the $2k_2$ component and is transferred across the spectra to the k_2 component. Since the k_2 -mode is simultaneously involved in the triad resonance, it interacts with k_1 and k_3 and transfers energy to the long wave components. When the near second harmonic resonances are accounted for, additional unstable energy is supplied by $2k_1$ and $k_1 + k_2$ to the primary modes k_1 and k_2 which then transfer that energy to the k_3 -mode.

This mechanism demonstrates that a significant amount of growth can occur for long wave components simply by accounting for second order resonant wave-wave interactions in unstable systems. The following chapter shall demonstrate that these types of interactions can be observed in physical experiments.

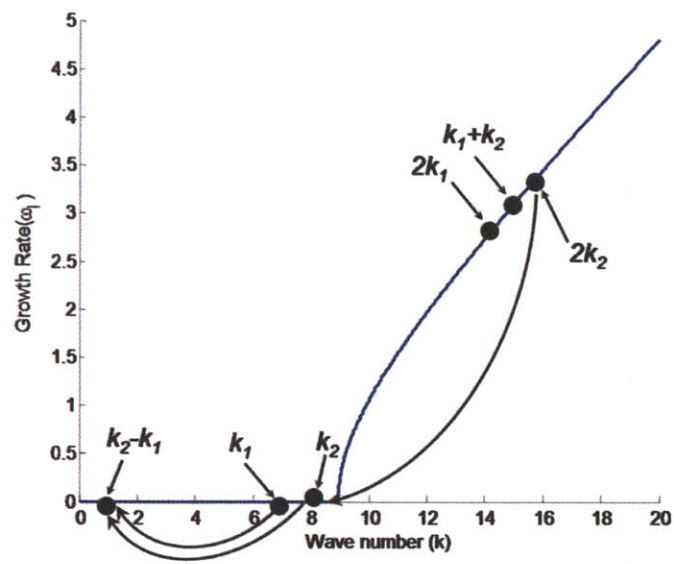


Figure 4-11: Energy transfer mechanism due to resonant interactions

Chapter 5

Comparisons to Experiments Containing Unstable Resonant Wave-Wave Interactions

The previous chapter demonstrated analytically and/or numerically the resonant wave-wave interactions and the affect of linear instabilities. In order to validate the theory and demonstrate the efficacy of these interactions in producing slug flow, it would be necessary to have an experimental comparison. However, a search of published literature showed that there was an inadequate collection of data containing wave spectra measurements of Kelvin-Helmholtz flows in horizontal rectangular channels. As a result, no direct comparison could be made.

As an alternative, it was rationalized that comparisons could be made against a similar two layer fluid flow which contained a different linear instability. The only difference would be that the dispersion relationship would take on a slightly different form from the Kelvin-Helmholtz instability.

The work of Jurman et al [10] experimentally examined shear-generated interfacial waves close to the Orr-Sommerfeld neutral stability condition. In that work, the authors designed a one-inch deep horizontal channel which had an air and glycerin-water solution flowing through it. This work provided spectral evolution of the interfacial waves and demonstrated that depending on the Reynolds number and void frac-

tion, nonlinear energy transfer occurred among various interfacial modes by several possible mechanisms. Bi-coherence spectra were provided which demonstrated strong coupling between the various interacting modes, though more explanation was needed to explain the exact underlying physical processes.

Since the current potential flow analysis was fundamentally unable to represent physics associated with shear instabilities in the fluid, it was necessary to apply a model to account for these affects. Song and Banner [18] utilized a slope coherent pressure forcing model of the form:

$$P_f = \beta \frac{\partial \eta}{\partial x}$$

which mimics wave instability due to shear velocity profiles. When this pressure forcing model was applied to the dynamic boundary conditions, a linear dispersion relationship of the form:

$$\begin{aligned} \omega^2 \left[\frac{R}{k \tanh(kh_u)} + \frac{1}{k \tanh(kh_l)} \right] \\ + \omega \left[\frac{-2U_u R}{\tanh(kh_u)} + \frac{-2U_l}{\tanh(kh_l)} + \frac{2ik^2}{Re} \left(\frac{N}{k \tanh(kh_u)} + \frac{1}{k \tanh(kh_l)} \right) \right] \\ + \left[\frac{(U_l k)^2}{k \tanh(kh_l)} + \frac{R(U_u k)^2}{k \tanh(kh_u)} - \frac{2ik^2}{Re} \left(\frac{NU_u}{\tanh(kh_u)} + \frac{U_l}{\tanh(kh_l)} \right) \right. \\ \left. - (1 - R) - \frac{k^2}{We} - ik\beta \right] = 0 \quad (5.1) \end{aligned}$$

is produced. As in the case of Kelvin-Helmholtz flows, the dispersion relationship is capable of admitting complex frequencies which cause the interfacial wave mode to grow exponentially with time.

The first trial that was considered had a gas Reynolds number of $R_g = \frac{\rho_g U_g h_g}{\mu_g} = 4000$ and a liquid Reynolds number of $R_l = \frac{\rho_g U_g h_g}{\mu_g} = 70$ near the inlet. The initial gas and liquid depths were $h_l = 0.65$ cm and $h_g = 1.89$ cm respectively. The liquid viscosity was $\mu_l = 9.5$ cP and the gas velocity was $2.9 \frac{m}{s}$. It was observed in the experiments that a dominant wave mode of wavelength $\lambda \approx 4.1$ cm grew until it achieve a limiting steepness of $\frac{a}{\lambda} \approx 0.005$. The measured wave spectra showed a large

amplitude, narrow banded peak around the dominant wave mode with a very small peak at the second harmonic of the primary mode. Time traces of the interfacial elevation show that set down occurs, dropping the mean water level by 0.02 cm.

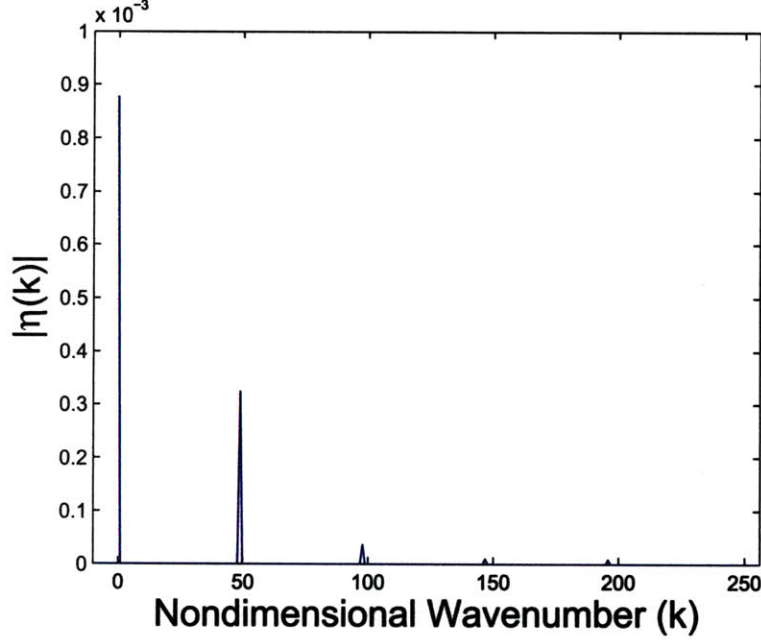


Figure 5-1: Dimensionless HOS simulation corresponding to Figure 3 from Jurman [10] with dominant wave mode $k = 49$

The HOS method developed in this paper was used to recreate these results as shown in Figure 5-1. The normal viscous stresses, described by Eqn. (2.7), were utilized in order to achieve proper Reynolds scaling and also to properly damp the short waves in the spectra as would be observed in the physical experiment.

Since the dominant wave mode was identified by Jurman to be caused by an Orr-Sommerfeld instability, it would not be possible to be predicted the unstable mode through the potential flow formulation. To account for this, the pressure forcing model was applied only to the experimentally observed dominant mode ($\lambda \approx 4.1\text{cm}$), creating an energy source to a single spectral mode. The simulation was initialized with a small disturbance at the dominant wave mode and the resulting forcing coefficient β was selected which produced an interfacial steepness of $\frac{a}{\lambda} = 0.005$. For this particular trial, the pressure forcing coefficient was found to be $\beta = 3.2056 \times 10^{-4}$ and

$L' = 2\text{m}$ (this value will be used for all trials in this chapter). With this coefficient, similar amplitudes were observed for both the primary peak and the higher harmonics as were seen by the measured wave spectra. In addition to this, the HOS method also predicted the correct set down of the mean liquid level. Based on these observations and comparisons to measurements, it seems that the pressure forcing model provides an adequate means for representing the shear generated energy input to the liquid. It is interesting to note that in this trial, no resonant conditions were satisfied. As a result the amplitude remains concentrated at the primary mode and with only small amplitudes being observed at its higher harmonics.

A more complicated flow was observed when the gas and liquid Reynolds were adjusted to $R_g = 5150$ and $R_l = 14$ respectively. The liquid depth was decreased to $h_l = 0.45\text{ cm}$ and the gas velocity was increased to $3.7\frac{\text{m}}{\text{s}}$. The liquid mixture was also changed such that the new viscosity was $\mu_l = 10\text{ cP}$. In this case, the experiments show that a similar dominant mode with wavelength $\lambda \approx 2.3\text{ cm}$ is observed to form and grow until it reaches some unique limiting steepness. However, in this trial a new subharmonic component forms at approximately half the frequency of the dominant mode. The amplitude of this mode grew with the primary mode, but was always of smaller amplitude. Set down was observed and appeared to be a function of fetch.

When the HOS method was run at these flow conditions, the experimental results were once again recreated with good agreement being observed as can be seen in Figure 5-2. For this trial, the pressure forcing coefficient was found to be $\beta = 3.8468 \times 10^{-4}$. It should be noted, that it was expected that the coefficient be slightly different from the previous trial because the flow properties (density and viscosity) were changed by a small margin. The fact that these two pressure forcing coefficients are of similar magnitude seems reasonable. Comparisons between the HOS simulation results and the experimental findings show the accurate prediction of the growth of a subharmonic mode at these flow conditions. In addition to this, similar set down is observed. The fact that the subharmonic develops is expected because the dispersion relationship shows that there is a second harmonic resonance condition which is satisfied at this trial's flow conditions. In this case, however, the resonance

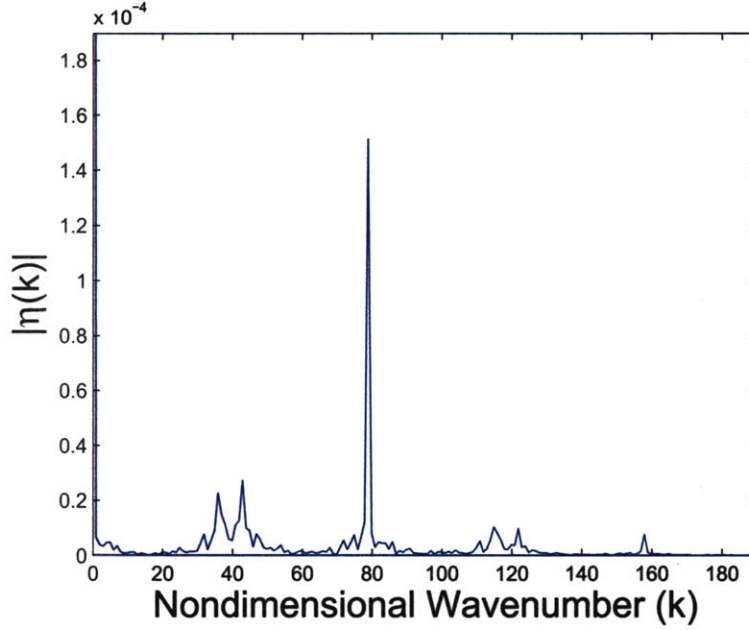


Figure 5-2: Dimensionless HOS simulation corresponding to Figure 7 from Jurman [10] with dominant wavemode $k = 79$

was between the dominant mode (k_1) and its subharmonic ($\frac{1}{2}k_1$). As in the unstable Kelvin-Helmholtz trials that were examined in Section 4.2, the resonant interactions allow for the energy supplied by the linear instability to be transferred across the spectra from short waves to longer waves.

The last trial considered was conducted with a gas and liquid Reynolds number of $R_g = 6300$ and $R_l = 5$ respectively. The liquid layer had a depth of $h_l = 0.44$ cm and a gas velocity of $U_u = 4.5 \frac{m}{s}$. The liquid mixture was adjusted such that the liquid viscosity was $\mu_l = 20$ cP. In this trial, a dominant wave appeared with wavelength $\lambda = 2.33$ cm. In addition to this, several sidebands appeared on either side of the dominant mode. This trial is unique because as the dominant wave-mode grows to a limiting steepness, new long waves appear to develop.

The HOS method was again used to recreate the experimentally observed phenomena as shown in Figure 5-3. In this trial, the pressure forcing coefficient is $\beta = 8.0141 \times 10^{-4}$. This value seems reasonable in comparison to the previous trials because the liquid viscosity is twice as large as the previous two trials. Comparisons

between the HOS simulation and the experimental findings show that the numerical method correctly predicted the growth of both the sidebands and long wave components. Similarly, the set down is in good agreement with the experiments. As in the

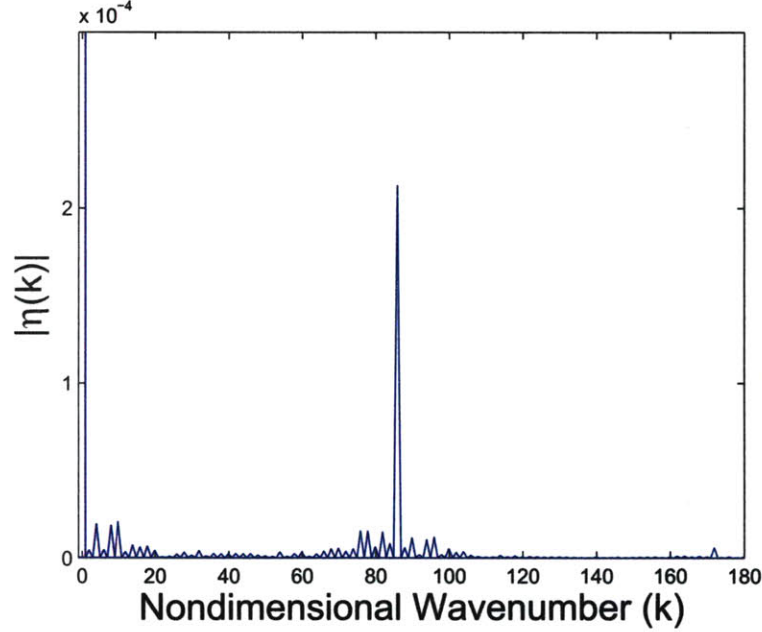


Figure 5-3: Dimensionless HOS simulation corresponding to Figure 9 from Jurman [10] with dominant wavemode $k = 86$

previous trial, the growth of the long waves is expected. These flow conditions admit both a second harmonic and a triad resonance. As in the previous trial, energy is transferred to a subharmonic mode; however in this case, that subharmonic mode is simultaneously involved in a triad resonance which results in the unstable energy being rapidly transferred through the subharmonic mode to the long wave components. This mechanism is analogous to the coupled resonances which were documented for the unstable Kelvin-Helmholtz flows in Section 4.2.

The findings in this chapter demonstrate that the unstable resonance which are predicted theoretically are physically realizable. They have been demonstrated as being strong and efficient mechanisms which are responsible for the transfer of energy across the wavenumber spectra.

Chapter 6

Discussion and Conclusions

This work examines the role that nonlinearity (in interfacial wave motion) has in the transition of a stratified two-fluid channel flow to unstable, large amplitude, long waves. Resonant wave-wave interactions are identified and it is found that specific sets of wavenumbers can become coupled producing rapid energy transfer among the resonant modes. Both numerical and analytical methods were developed using high order perturbation schemes to study these nonlinear interactions. It is found that two classes of resonances can be observed depending on if the linear solution is stable or unstable to the Kelvin-Helmholtz mechanism.

If all of the modes in the triad are stable to the Kelvin-Helmholtz instability, the energy in the triad is conserved. These oscillations are periodic with time and have maximum amplitudes that are of the same order as the initial conditions of the two first order wave components. If the components are detuned away from the exact resonance condition, the maximum amplitude of the second order wave mode (the difference component) decreases. Analytical solutions were developed to demonstrate the effects of detuning and were found to be in good agreement with the numerical solution. When viscosity is included, the large amplitude response of the difference component could still be observed; however, all waves in the triad eventually decay to zero, with the short waves decaying the fastest.

If any of the modes in the triad are linearly unstable to the Kelvin-Helmholtz mechanism, it is possible for the response amplitudes to be orders of magnitude

larger than the stable resonance case. Triad resonance could occur involving one unstable mode near the neutral point of the dispersion curve, and two other modes in the stable region. The unstable mode was found to grow quickly due to the linear instability, while simultaneously interacting and transferring energy to the two other modes through the triad resonance. It is possible for this triad resonance to generate a large amplitude, long wave. Second harmonic resonances were also observed between a mode near the neutral point and its second harmonic. The second harmonic, which was always linearly unstable, transferred significant amounts of energy to the primary wave component creating large amplitude oscillations of both of these interacting modes. When the mode near the neutral point is involved simultaneously in both a second harmonic resonance and a triad resonance, then it is possible for large amounts of energy to be transferred from the unstable second harmonic, to the primary wave, which then directly transfers the energy to the long wave components through the triad resonance. This cascade of energy through the coupled triad and second harmonic resonance was found to be strong and highly efficient at creating large amplitude long waves.

Qualitative comparisons were made with published experimental findings of a weak Orr-Sommerfeld instability in a stratified horizontal channel flow. A pressure forcing model was generated to account for the linear Orr-Sommerfeld instability and good agreement was observed between numerical solutions and the experimental results. It is observed that these theoretically predicted resonant interactions are present in physical systems are responsible for the transfer of energy across the wave spectrum.

This work is directly applicable to the predication of slug formation in horizontal stratified flows. Traditional methods utilize modified forms of the Kelvin-Helmholtz linear stability theory to predict the growth or large wave disturbances; however, in many cases flows which are predicted to be stable are found to produce liquid slugs. By neglecting the role of nonlinearity, these resonant interactions are not accounted for making it impossible to predict the formation of the large amplitude, long waves observed in this work.

While a rich collection of physics is found to occur with a small set of discrete

wave modes, it is of interest to extend this work to the more complicated case of a broadband spectrum. In doing so, there will be more unstable modes capable of transferring energy to the stable wave modes making it possible for the formation of breaking waves and slugs to occur. The resulting interfacial dynamics will become significantly more complicated by the presence of many sets of coupled resonant interactions occurring simultaneously. Microwave breaking will occur among the capillary waves and need to be accounted for in order for the accuracy of the numerical method to be maintained.

Future work should also include the development of more advanced analytical methods capable of describing the resonant wave-wave interactions in a flow where the wave modes have strong linear instabilities ($O(\omega_I) \gg 1$). Currently, methods (such as the method of multiple scales) are only applicable for examining weak instabilities and are limited to the initial growth phase. This work demonstrated that there is a need to understand the interfacial evolution over a significantly longer period of time. Such analytical methods could prove to be valuable in developing stability criteria which could be applied directly in the design of multiphase engineering systems.

It is also important to consider in future work the effects of higher order nonlinearities. This work demonstrated new physics from second order nonlinearities. Additional resonances would be found in higher order solutions. Frequency-amplitude interactions have been documented to occur at third order which may cause the response and resonance conditions to adjust as the amplitudes become large.

While considerable insight can be obtained from weakly nonlinear analysis, it is likely that in order to accurately resolve slug formation, fully nonlinear computational methods will become necessary. As the waves become steeper and come close to bridging the pipe diameter, the viscous and turbulent effects may become dominant. Direct numerical simulations of the fully nonlinear governing equations will provide the necessary understanding of the small scale interactions in the flow and provide insights into the detailed turbulent structure.

Appendix A

Convergence Test Results

k/Grid Points	Spatial Points			
	32	64	128	256
1	-4.5826E-06	-4.5826E-06	-4.5826E-06	-4.5826E-06
2	3.3266E-05	3.3266E-05	3.3266E-05	3.3266E-05
3	9.6666E-06	9.6666E-06	9.6666E-06	9.6666E-06
4	4.0944E-05	4.0944E-05	4.0944E-05	4.0944E-05
5	1.4149E-05	1.4149E-05	1.4149E-05	1.4149E-05

Table A.1: Convergence of the Frequency (ω_R) with Grid Refinement

k/Iter. Period	Time Steps per Wave Period			
	32	64	128	256
1	-4.5826E-06	-4.5826E-06	-4.5826E-06	-4.5826E-06
2	3.3266E-05	3.3266E-05	3.3266E-05	3.3266E-05
3	9.6666E-06	9.6666E-06	9.6666E-06	9.6666E-06
4	4.0944E-05	4.0944E-05	4.0944E-05	4.0944E-05
5	1.4149E-05	1.4149E-05	1.4149E-05	1.4149E-05

Table A.2: Convergence of the Frequency (ω_R) with Time Step Refinement

k/Grid Points	Spatial Points			
	32	64	128	256
1	3.1640E-05	3.1681E-05	3.1786E-05	3.1796E-05
2	6.2842E-05	6.3146E-05	6.3240E-05	6.3410E-05
3	9.3965E-05	9.4224E-05	9.4625E-05	9.4558E-05
4	1.2418E-04	1.2435E-04	1.2500E-04	1.2509E-04
5	1.5477E-04	1.5453E-04	1.5531E-04	1.5547E-04

Table A.3: Convergence of the Growth Rate (ω_I) with Grid Refinement

k/Iter. Period	Time Steps per Wave Period			
	32	64	128	256
1	3.6904E-05	3.1681E-05	3.1480E-05	3.1456E-05
2	7.3665E-05	6.3146E-05	6.2774E-05	6.2728E-05
3	1.1004E-04	9.4224E-05	9.3599E-05	9.3526E-05
4	1.4592E-04	1.2435E-04	1.2379E-04	1.2369E-04
5	1.8178E-04	1.5453E-04	1.5384E-04	1.5372E-04

Table A.4: Convergence of the Growth Rate (ω_I) with Time Step Refinement

Bibliography

- [1] Alam, M.-R., Liu, Y. & Yue, D. K. P. 2009 Bragg resonance of waves in a two-layer fluid propagating over bottom ripples. Part II. Numerical simulations. *J. Fluid Mech.* (in press).
- [2] Barnea, D., Taitel, Y., 1993. Kelvin-Helmholtz stability criteria for stratified flow: viscous versus non-viscous(inviscid) approaches. *Int. J. Multiphase Flow* 19, 639-649.
- [3] Benney, D.J. 1962. "Non-linear gravity wave interactions." *J. Fluid Mech.* 14, 577-584.
- [4] Bontozoglou, V., and Hanratty, T.J., "Capillary gravity Kelvin-Helmholtz waves close to resonance," *J. Fluid Mech.*, 217, 71 (1990)
- [5] Dommermuth, D. G. Yue, D.K.P. 1987 A high-order spectral method for the study of nonlinear gravity waves. *J. Fluid Mech.* vol. 184, pp. 267-288.
- [6] Fan, Z., Lusseyran, F. and Hanratty, T. J. 1993a "Initiation of slugs in horizontal gas-liquid flows." *AIChE J.* 39, 1741-1753.
- [7] Funada, T., Joseph, D.D., 2001. Viscous potential flow analysis of Kelvin-Helmholtz instability in a channel. *J. Fluid Mech.* 445, 263-283.
- [8] Janssen, P. A. 1986 "The period-doubling of gravity-capillary waves." *J. Fluid Mech.* 172, 531-546.
- [9] Janssen, P. A. 1987 "The initial evolution of gravity-capillary waves." *J. Fluid Mech.* 184, 581-597.
- [10] Jurman, L. A., Deutsch, S. E., and McCready, M. J. 1992. Interfacial mode interactions in horizontal gas-liquid flows. *J. Fluid Mech.* 238, 187-219.
- [11] Kordyban, E.S. and Ranov, T., "Mechanisms of slug formation in horizontal two-phase flow," Trans. ASME, *J. Basic Eng.*, 92, 857 (1970).
- [12] Lin, P.Y., and Hanratty, T.J., 1986. Prediction of the initiation of slugs with linear stability theory. *Int. J. Multiphase Flow* 12, 79-98.
- [13] Longuet-Higgins, M. S. 1962 Resonant interactions between two trains of gravity waves. *J. Fluid Mech.* 12, 321-332.

- [14] Mata. C., Pereyra, E., Trallero, J.L., Joseph, DD 2002. Stability of stratified gas-liquid flows. *Int. J. Multiphase Flow* 28, 1249-1268.
- [15] McGoldrick, L. 1965 Resonant interactions among capillary-gravity waves. *J. Fluid Mech.* 21, 305-331.
- [16] Mishima, K., and M. Ishii, "Theoretical prediction of the onset of horizontal slug flow," *J. Fluids Eng.*,102,446 (1980).
- [17] Phillips. O. M. 1960. "On the dynamics of unsteady gravity waves of finite amplitude. Part 1. The elementary interactions," *J. Fluid Mech.* 9, 193-217.
- [18] Song. J.-B., and M.L. Banner, 2002: On determining the onset and strength of breaking for deep water waves. Part II: Influence of wind forcing and surface shear. *J. Phys. Oceanogr.*, 32,2541-2558.
- [19] Taitel,Y., and Dukler, A.E., 1976. "A model for predicting flow regime transition in horizontal and near horizontal gas-liquid flow." *AIChE J* 22, 47-55 (1976).
- [20] Wallis. G.B., and Dobson, J.E. "The onset of slugging in horizontal stratified air-water flow," *Int. J. Multiphase Flow*,1,173(1973).